

# Numerical investigation of deformation mechanics in fold-and-thrust belts: Influence of rheology of single and multiple décollements

Jonas B. Ruh,<sup>1</sup> Boris J. P. Kaus,<sup>2</sup> and Jean-Pierre Burg<sup>1</sup>

Received 18 October 2011; revised 14 March 2012; accepted 20 March 2012; published 8 May 2012.

[1] Thin-skinned fold-and-thrust belts related to convergence tectonics develop by scraping off a rock sequence along a weaker basal décollement often formed by water-saturated shale layers or low-viscosity salt horizons. A two-dimensional finite element model with a viscoelastoplastic rheology is used to investigate the structural evolution of fold-and-thrust belts overlying different types of décollements. In addition, the influence of multiple weak layers in the stratigraphic column is studied. Model shale décollements are frictional, with lower friction angles as the cover sequence. Model salt layers behave linear viscous, due to a lower viscosity as the cover sequence, or with a power law rheology. Single viscous décollement simulations have been compared to an analytical solution concerning faulting versus folding. Results show that fold-and-thrust belts with a single frictional basal décollement generate thrust systems ramping from the décollement to the surface. Spacing between thrust ramps depends on the thickness of the cover sequence. The structural evolution of simulations with an additional low-frictional layer depends on the strength relationship between the basal and the intersequential décollement. Tectonic underplating and antiformal stacking occur if the within-sequence décollement is weaker. In the frontal part of models, deformation is restricted to the upper part and imbrication occurs with a wavelength depending on the depth of the intermediate weak layer. “Salt” décollement with a viscosity of  $10^{18}$  Pa·s leads to isolated box folds (detachment folds). Multiple salt layers ( $10^{18}$  Pa·s) result in long-wavelength folding. Our results for both frictional and viscous décollements are in bulk agreement with the Mohr-Coulomb type, critical wedge theory.

**Citation:** Ruh, J. B., B. J. P. Kaus, and J.-P. Burg (2012), Numerical investigation of deformation mechanics in fold-and-thrust belts: Influence of rheology of single and multiple décollements, *Tectonics*, 31, TC3005, doi:10.1029/2011TC003047.

## 1. Introduction

[2] Fold-and-thrust belts have been within the scope of intense industrial and academic interest for several decades [e.g., Boyer and Elliott, 1982; McClay, 1992]. They are reported in contrasting tectonic settings such as passive margins, where they are gravity driven, and convergent zones such as mountain forelands and submarine accretionary wedges. In this study, we focus on the thin-skinned deformation of fold-and-thrust belts related to convergent plate boundaries. They develop by scraping off crustal material along a major décollement over a relatively rigid basement/subducting plate. Typically, such décollement

zones are weaker than the bulk of the deforming rock pile and often consist of a viscous salt layer or more or less water saturated, occasionally overpressured shale [e.g., Cooper, 2007; Morley et al., 2011]. Sliding of an evolving fold-and-thrust belt on a décollement depends on the stresses acting on the weak layer and its shear resistance. Therefore, the style of thin-skinned deformation is strongly dependent on the physical properties of the weak, major décollement layers.

[3] Submarine accretionary wedges like Barbados [Westbrook et al., 1988], the Makran [Platt et al., 1985; Grando and McClay, 2007] and the South Caspian Sea [Berberian, 1983] are typical examples for fold-and-thrust belts with shale as décollement horizons in convergent zones. Shale-related fold-and-thrust belts are also known from retroarc settings like the sub-Andean ranges in Argentina [Echavarría et al., 2003]. Fold-and-thrust belts with décollements within salt layers often occur in front of orogenic belts. The Jura Mountains [Laubscher, 1992; Sommaruga, 1999], the Salt Range and Potwar Plateau [Baker et al., 1988; Grelaud et al., 2002; McClay et al., 2004], the Pyrenees [Bourrouilh et al., 1995], the Parry Island Fold Belt

<sup>1</sup>Geological Institute, ETH Zurich, Zurich, Switzerland.

<sup>2</sup>Institute of Geosciences, Johannes Gutenberg University Mainz, Mainz, Germany.

Corresponding author: J. B. Ruh, Geological Institute, ETH Zurich, Sonneggstr. 5, CH-8092 Zurich, Switzerland. (jonas.ruh@erdw.ethz.ch)

Copyright 2012 by the American Geophysical Union.  
0278-7407/12/2011TC003047

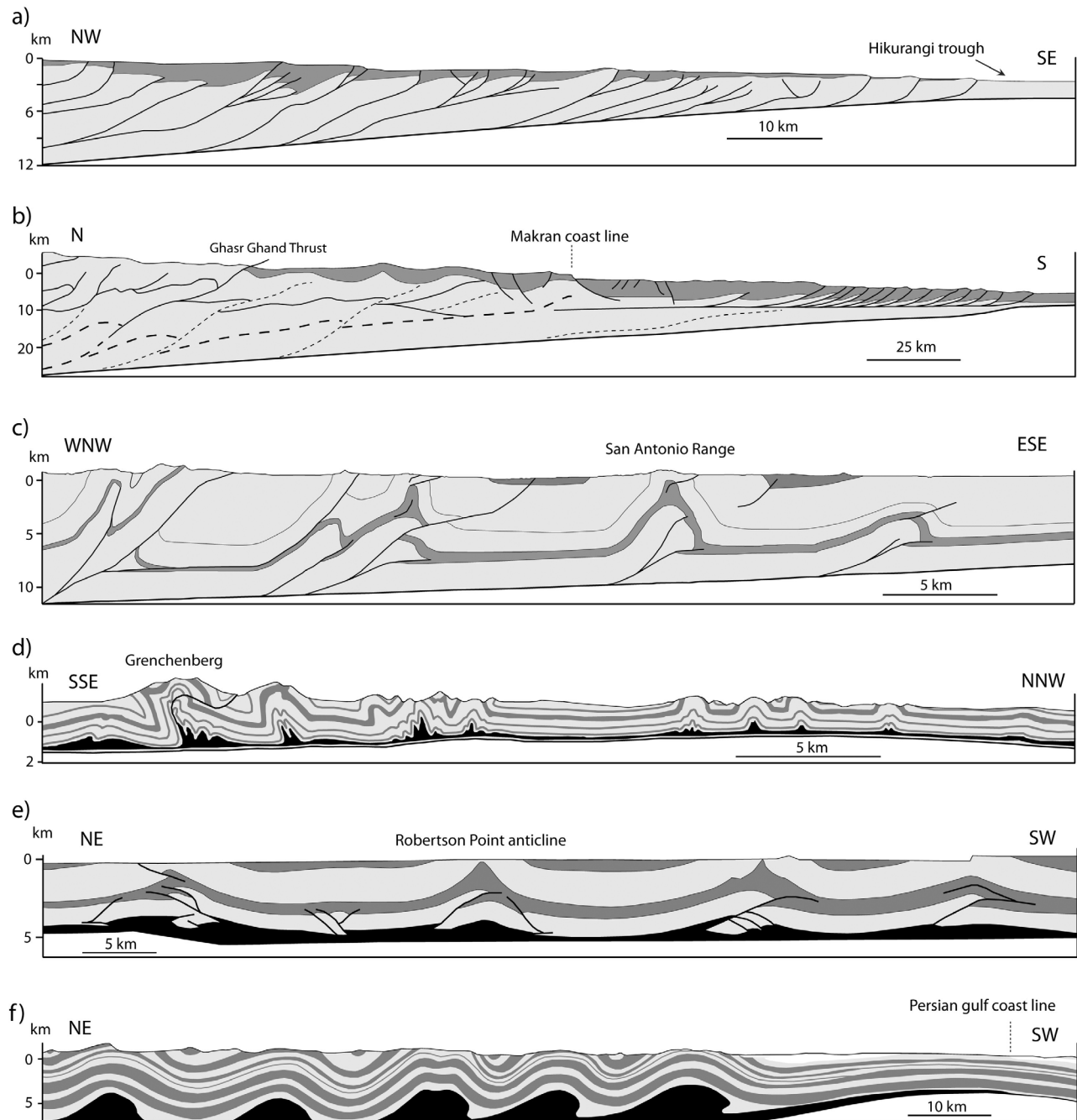


**Figure 1.** Profiles of selected fold-and-thrust belts with different décollement types. (a) One frictional décollement: Hikurangi subduction margin, NE New Zealand (adapted from *Barnes et al.* [2010]), where ramps splay up to the surface. (b) Two or more frictional décollements: Makran accretionary wedge, SE Iran (adapted from *Burg et al.* [2011]). With duplex structures: (c) multiple shale décollements: sub-Andean thrust belt, Argentina (adapted from *Echavarría et al.* [2003]). Spaced ramp anticlines: (d) one salt décollement: Faltenjura, NW Switzerland (adapted from *Buxtorf* [1916]), with narrow symmetrical anticlines and broad synclines. (e) Two salt décollements: Parry Island fold belt, Arctic Canada (adapted from *Harrison* [1995]). (f) Two or more salt décollements: southwestern simply folded zone in Zagros, SW Iran (adapted from *Hessami et al.* [2001]).

[*Harrison, 1995*] and the Zagros folded belt [*Mouthereau et al., 2006*] are typical examples. Cross sections illustrate the geometrical variability of these fold-and-thrust belts (Figure 1), which all involve thin-skinned tectonics in

unmetamorphosed to low-grade metamorphic sedimentary sequences [*Poblet and Lisle, 2011*].

[4] Although the large-scale mechanics of accretionary wedges and foreland fold-and-thrust belts are comparable

(sediments are decoupled from and pushed over a rigid basement by a moving backstop), the difference in structural evolution and deformation style strongly depends on whether a salt or a shale layer forms the décollement level, as replicated in many analog modeling studies. In such studies, shale décollements with a frictional boundary condition are mimicked by glass beads or a foil between the rigid basement and the deforming sand pile. Viscosity salt layers are simulated by low-viscosity silicon or honey [Storti and McClay, 1995; Costa and Vendeville, 2002; Bahroudi and Koyi, 2003; Bonini, 2007]. In numerical modeling studies, weak shale décollements are simulated by a layer with a lower Mohr-Coulomb failure criterion than the wedge-forming material [Selzer et al., 2007; Stockmal et al., 2007; Simpson, 2011]. Ings and Beaumont [2010] treat shale layers as viscoplastic Bingham fluids [Bingham, 1922]. Salt décollements are defined by a layer of much lower viscosity than the overlying material with linear [Simpson, 2010; Yamato et al., 2011] or non-Newtonian rheology [Chemia et al., 2009; Li et al., 2012].

[5] Besides the type of décollement, other important characteristics influence the structural evolution of fold-and-thrust belts. The presence of weak layers within the rock sequence affects the thin-skin deformation style, independent of whether salt or shale makes the décollement. In submarine accretionary wedges, multiple, often overpressured shale layers are common. An example is the Makran accretionary wedge (Figure 1b), where mud volcanoes collect overpressured mud horizons at shallow depth in the wedge sedimentary pile [Schlüter et al., 2002; Burg et al., 2011]. In the Parry Island and Zagros fold belts (Figures 1e and 1f), where the basal décollement is in evaporite, additional thin evaporite and shale layers occur within the stratigraphy [Motiei, 1993; Harrison, 1995]. These could favor folding rather than faulting because intermediate décollements allow flexural slip [Yamato et al., 2011].

[6] One goal of this study is to constrain numerically our understanding of the influence of the décollement type on the structural evolution of a compressional fold-and-thrust belt. Numerical studies of the evolution of fold-and-thrust belts already exist, but they focused either on purely viscous or purely frictional décollements, rarely comparing these two types [Simpson, 2009]. Comparison is however important because the previous studies used different implementations and setups, which impedes direct assessment of the respective results. Another aim of this paper is to investigate the impact of multiple weak layers subsequently forming duplex structures within the thin-skinned stratigraphy. The role of several weak horizons has been investigated in few analog [e.g., Konstantinovskaya and Malavieille, 2011] and numerical studies [e.g., Yamato et al., 2011]. Building on these studies, ours is one of the first to implement frictional intermediate décollements [Stockmal et al., 2007] and the first to investigate the difference between single and multiple, viscous and frictional décollements using the same setup and analytic procedures. To achieve these aims, an incompressible 2-D numerical code, based on the Finite Element Method with viscoelastoplastic rheology, is employed. Finally, we use analytical approximations, based on the critical wedge theory, to explain the overall

characteristics of the model results related to both décollement types, frictional and viscous.

## 2. Mechanics of Shale and Salt Décollements and Structural Characteristics of Related Fold-and-Thrust Belts

### 2.1. Frictional Shale Décollement

[7] We treat shale as a purely frictional material, in contrast to a viscoplastic Bingham material, to make this study applicable to the boundary conditions of the critical wedge theory [Wang et al., 1980; Saffer et al., 2001; Kopf and Brown, 2003; Takahashi et al., 2007]. This implies a frictional resistance to sliding along a potential shale décollement. The relative weakness that prompts shale to act as décollement is largely due to high pore pressures resulting from burial below impermeable layers. An increase of pore pressure reduces the yield strength of rocks [Fischer and Paterson, 1989]. Consequently, the frictional resistance along such a décollement is defined by the yield strength of the overpressured shale. The yield strength depends on the friction angle  $\varphi$ , the cohesion  $C_0$ , the stress in normal direction to the fault plane  $\sigma_N$  and the fluid pressure  $P_f$

$$\tau = (\sigma_N - P_f) \cdot \tan \varphi + C_0 \quad (1)$$

[8] To simplify equation (1), one can eliminate the fluid pressure term and introduce a term for the decreased friction angle of the base layer,  $\varphi_b$ , which is used to calculate the basal yield stress  $\tau_b$

$$\tau_b = \sigma_N \cdot \tan \varphi_b + C_0 \quad (2)$$

[9] The mechanics of a wedge evolving over a frictional base are classically and extensively explained by the critical wedge theory [Davis et al., 1983; Dahlen et al., 1984]. The evolution of a fold-and-thrust belt is compared to the evolution of a pile of sand or snow pushed in front of a bulldozer along a plane with an inclination angle  $\beta$ . The exact solution of the noncohesive critical wedge equation yields the total taper ( $\alpha + \beta$ , where  $\alpha$  is the surface angle), which is a function of the base dip angle  $\beta$ , the internal strength of the deforming rock pile and the strength of the basal layer (Figure 2). According to the analytical solution, every wedge with given internal and basal strength and a defined base angle exhibits two critical total taper angles. Between these two angles, the wedge is considered to be stable. Below the minimum critical taper, thrusting thickens the rear of the wedge in order to increase the surface slope toward a stable taper. When the minimum critical taper is reached, the wedge accretes new material at its toe to sustain its stable surface angle. If the total taper exceeds the maximum critical taper, the wedge fails along normal faults to decrease the surface slope angle toward a stable attitude. For wedges with a frictional décollement, the cross-sectional taper and the internal deformation are independent of both the velocity of the basement relative to the rigid backstop and the thickness of the weak frictional layer.

[10] The structural characteristics of fold-and-thrust belts with a frictional boundary at their base can be best understood

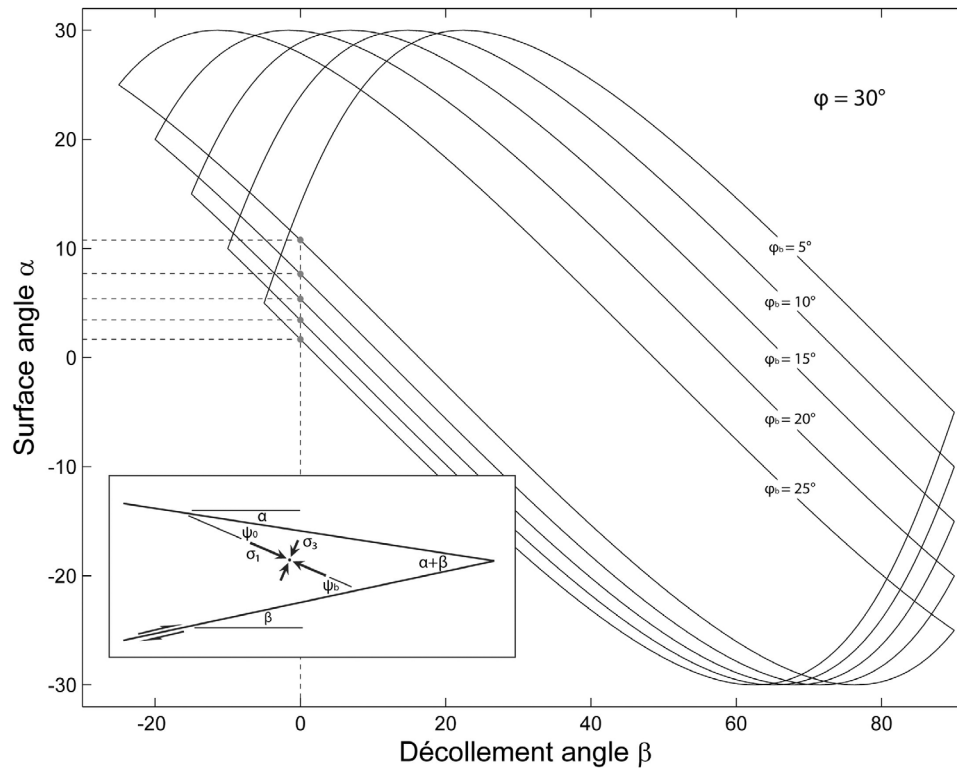


**Figure 2.** Flounder diagrams of the stability of frictional wedges with an internal friction angle  $\varphi = 30^\circ$  and basal friction angles  $\varphi_b$  from  $5^\circ$  to  $25^\circ$  [Davis *et al.*, 1983] relating minimal and maximal critical surface tapers to dip angle  $\beta$  of the basal décollement (every point within the flounder-shaped area is stable, points outside are unstable). Dots show minimum critical surface angles for a horizontal décollement ( $\beta = 0^\circ$ ) for different friction angles in the basal décollement. The bottom left inset defines angles  $\alpha$ ,  $\beta$ ,  $\psi_b$ ,  $\psi_0$  in a critical wedge and related principal stresses  $\sigma_1$ ,  $\sigma_3$  in two dimensions.

by studying accretionary wedges. Total tapers of accretionary wedges reported in the literature vary strongly, from  $2.9^\circ$  for the Makran to  $13.5^\circ$  for the Chile margin [Saffer and Bekins, 2006, and references therein]. This variability is attributed to the relation between the internal and basal strength and the fluid pressure.

[11] Thrusts are usually verging toward the toe (Figure 1a). Thrust sheets are developing sequentially (i.e., forward with respect to the sense of general thrusting) as the wedge grows by accumulating new material at its toe and thus building a new frontal thrust. The size of the thrust sheets strongly depends on the thickness of the incorporated rock sequence. Backthrusts appear at the rear of accretionary wedges when deformation reaches the internal parts [Poblet and Lisle, 2011]. Many accretionary wedges exhibit large-scale underplating, i.e., sediments are thrust below an evolving wedge [e.g., Platt *et al.*, 1985]. Underplating leads to increasing confining pressures due to increasing load of the thickening wedge; the subsequent formation of duplex thrust sheets [Glodny *et al.*, 2005] leads to faster surface uplift at the rear of the wedge [Ellouz-Zimmermann *et al.*, 2007].

## 2.2. Viscous Salt Décollement

[12] If the main décollement is formed by a salt layer, it is viscous [Nettleton, 1934]. A wealth of studies investigated the rheology of salt, defining its viscosity to be Newtonian (linear relation between stress and strain rate) or non-

Newtonian (power law relation between stress and strain rate) [Spiers *et al.*, 1990; Chemia *et al.*, 2008, 2009; Urai *et al.*, 2008; Marques *et al.*, 2011]. In this study, we take both rheologies into account to model salt décollements.

[13] The resistance to shearing of a purely viscous material is defined by the shear stress of a viscous fluid  $\tau_b$ , which is (for a Newtonian fluid) linearly proportional to the velocity gradient within the viscous layer and to its viscosity, and inverse proportional to the layer thickness [Turcotte and Schubert, 2002]. This is expressed by

$$\tau_b = \eta \cdot \frac{\Delta u}{h}, \quad (3)$$

where  $\eta$  is the dynamic viscosity and  $\Delta u$  the difference in horizontal velocity along the vertical thickness  $h$  of the viscous layer. In contrast to frictional décollements, there is no failure since a low-viscosity fluid is easily sheared and flows. Equation (3) shows that the shear stress in a viscous layer, which influences the wedge formation, depends on the thickness, the viscosity and the difference of compression rate between the top and the bottom of the viscous layer. This “salt behaviour” contrasts with the “shale behaviour” (see equation (2)).

[14] Another difference verified by equations (2) and (3), where  $\sigma_N$  defines the normal pressure state, is the influence of the overlying rock sequence: in the case of a frictional

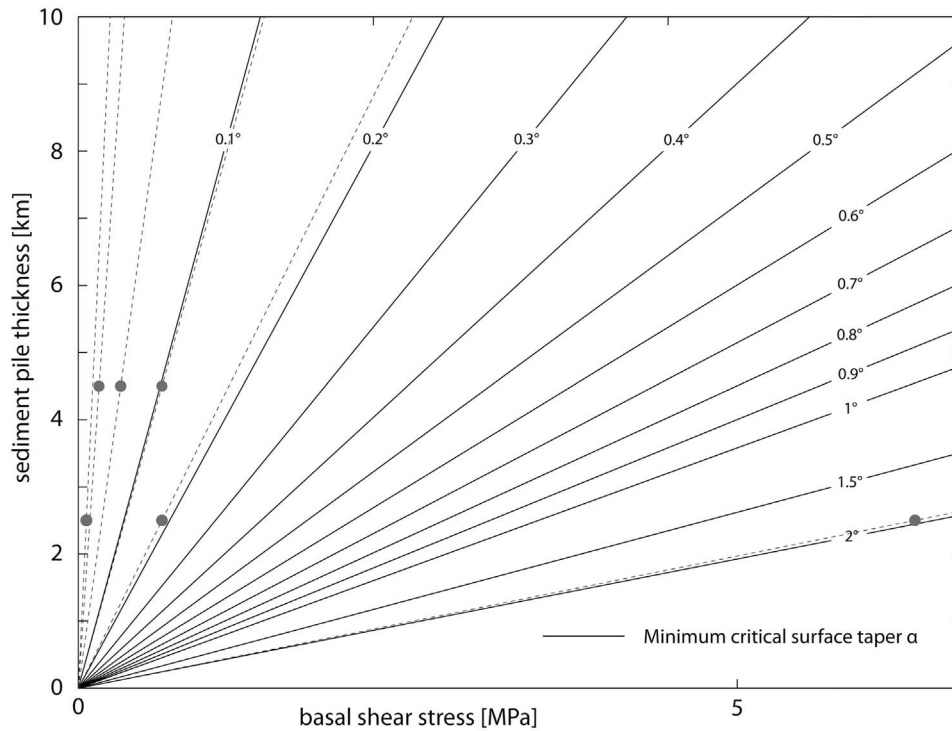


**Figure 3.** Theoretical surface slopes for wedges overlying a horizontal salt décollement. Values for resulting surface slope depend on basal shear stress and overburden thickness (after equation (3) by *Davis and Engelder* [1985]). Gray dots: simulations carried out in this study. Dashed lines: taper angles according to gray dots.

décollement, the strength of the décollement layer and the strength of the overlying sequence both depend on the mass of the hanging wall. This leads to the fact that theoretical surface taper angles of wedges evolving on frictional décollements are independent of the thickness of the moving rock sequence [*Dahlen et al.*, 1984, equation 17]. In the case of a viscous décollement, the strength of the basal layer is pressure independent (see equation (3)), in contrast to the pressure-dependent strength of the overlying rock sequence. As a consequence, the overburden thickness influences the wedge shape. Applying equation (3) from *Davis and Engelder* [1985] illustrates the theoretical surface slope angles of a wedge on a horizontal viscous décollement depending on the thickness of the cover sequence and the shear stress for the viscous layer, calculated by our equation (3) (Figure 3).

[15] Several parameters defining the shear stress in a viscous décollement can be estimated empirically: the thickness of salt layers is known from drilling logs and seismic profiles and by GPS measurements constrain the velocity of active plate convergence [e.g., *Sommaruga*, 1997; *Vernant et al.*, 2004]. The viscosity of salt is more debatable, due to the wide range of published values, from  $2.7 \cdot 10^{10}$  to  $10^{23}$  Pa·s for Newtonian and non-Newtonian rheology, where most values fall between  $10^{17}$  and  $10^{20}$  Pa·s [*Mukherjee et al.*, 2010, and references therein].

[16] Shear stresses defined by equation (3) can be very low in weak layers, so that fold-and-thrust belts on a viscous décollement have cross-sectional tapers much narrower than for other wedges [*Davis and Engelder*, 1985]. Therefore, a wide fold belt can evolve as minor fold growth at the rear already results in a surface slope larger than the minimum

critical taper. The deformation front is pushed further away from the backstop. In the Jura (Figure 1d) for example, narrow anticlines are clustered in the South (Faltenjura) and form box folds separated by flat-bottomed, broad synclines in the North (Plateaujura) [*Sommaruga*, 1997; *Pfiffner*, 2009]. An example for a salt-related fold-and-thrust belt with several weak zones is the Zagros folded belt [*Motiei*, 1993]. The simply folded zone of Zagros (Figure 1f) is characterized by periodic, symmetrical and open anticlines and synclines with an average wavelength of  $\sim 14.5$  km [*Yamato et al.*, 2011].

### 3. Model Setup

#### 3.1. Governing Equations

[17] The mechanical model is based on the equations for conservation of momentum

$$-\frac{\partial P}{\partial x_i} + \frac{\partial \tau_{ij}}{\partial x_j} = \rho g_i \quad (4)$$

and the conservation of mass for an incompressible case

$$\frac{\partial u_i}{\partial x_i} = 0, \quad (5)$$

where  $P$  is pressure ( $P = -\frac{\sigma_{ii}}{3}$ ),  $\sigma_{ij}$  the stress tensor,  $\tau_{ij}$  the deviatoric stress tensor ( $\tau_{ij} = \sigma_{ij} + P$ ),  $u_i$  the velocity ( $u_1 = u_x$ ,  $u_2 = u_z$ ),  $x_i$  the spatial coordinates ( $x_1 = x$ ,  $x_2 = z$ ),  $\rho$  the density and  $g_i$  the gravitational acceleration ( $g_1 = 0$ ,  $g_2 = 9.81 \text{ m/s}^2$ ).

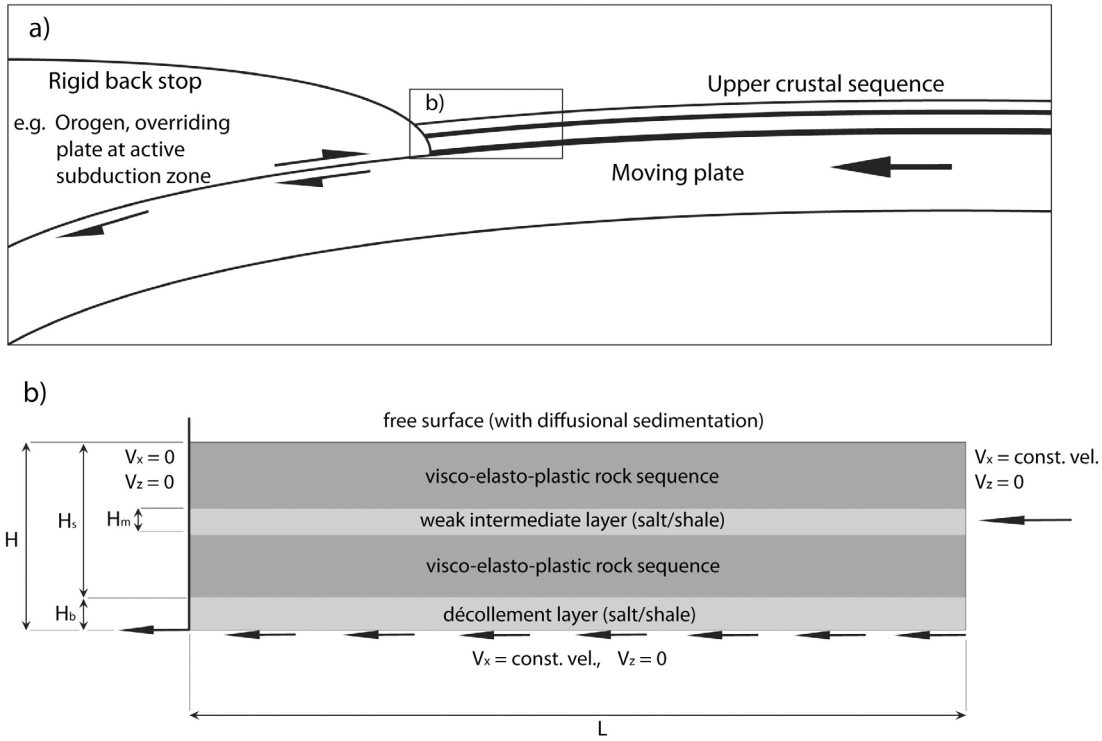


**Figure 4.** (a) Model setup in a larger tectonic context. Rigid backstop appears as overriding plate at convergent subduction zone with accretionary wedge or as existing orogen or Molasse basin in foreland-type fold-and-thrust belts. (b) Model setup. Parameters defined in Table 1. Boundary conditions are no-slip at the left side, constant velocity in the horizontal direction at the right side and at the bottom and free surface at the top boundary.

[18] The model follows a Maxwell viscoelastoplastic shear rheology, defined by

$$\dot{\epsilon}_{ij} = \frac{1}{2\eta} \tau_{ij} + \frac{1}{2G} \frac{D\tau_{ij}}{Dt} + \dot{\lambda} \frac{\partial Q}{\partial \sigma_{ij}}, \quad (6)$$

where  $\eta$  is the effective viscosity,  $G$  the elastic shear modulus,  $t$  time,  $\dot{\lambda}$  the plastic multiplier and  $Q$  the plastic flow potential [Moresi *et al.*, 2007]. The corotational derivative of the deviatoric stress tensor after Jaumann is defined by

$$\frac{D\tau_{ij}}{Dt} = \frac{\partial \tau_{ij}}{\partial t} + u_k \frac{\partial \tau_{ij}}{\partial x_k} - W_{ik} \tau_{kj} + \tau_{ik} W_{kj}, \quad (7)$$

where  $W$  is the vorticity  $\left(W_{ij} = \frac{1}{2} \left( \frac{\partial u_i}{\partial x_j} - \frac{\partial u_j}{\partial x_i} \right)\right)$ .

[19] If differential stresses exceed the yield stress, rocks fail plastically according to the Mohr-Coulomb failure criterion. After Vermeer and De Borst [1984], the yield function in 2-D is defined as

$$F = \tau^* - \sigma^* \sin \varphi - C \cdot \cos \varphi \quad (8)$$

and the plastic flow  $Q$  as

$$Q = \tau^* - \sigma^* \sin \psi, \quad (9)$$

where  $\tau^* = \sqrt{\left(\frac{\sigma_{xx} - \sigma_{zz}}{2}\right)^2 + \sigma_{xz}^2}$  and  $\sigma^* = -\frac{1}{2}(\sigma_{xx} + \sigma_{zz})$ .  $C$  is the cohesion,  $\varphi$  the friction angle and  $\psi$  the dilation angle, which is zero in incompressible systems.

### 3.2. Numerical Implementation

[20] The governing equations described in the previous section are solved numerically by discretizing the time derivative of equation (6) in an implicit manner. The rheological behavior is initially viscoelastic. If stresses exceed the yield stress ( $F(\tau_{ij}) > 0$ ), effective viscosities are decreased until the maximum stresses are at the yield stress ( $F = 0$ ). The discretized system of equations is solved with the finite element code MILAMIN\_VEP [e.g., Kaus, 2010], which employs techniques described in Dabrowski *et al.* [2008] to speed up the matrix assembly. Plasticity is solved iteratively until either the error is below a critical value or after a given amount of iteration steps. Quadrilateral elements, bilinear shape functions for velocity and a constant shape function for pressure ( $Q_1P_0$ ) in combination with direct solvers were used in all simulations of this study.

### 3.3. Boundary Conditions and Initial Geometry

[21] The same velocity boundary conditions have been applied to all simulations presented here. They simulate the mechanics of convergent plate boundaries where a rigid backstop scrapes upper levels of the crust off a rigid moving “plate” (Figure 4a). This is comparable to setups of analog models, where a rough sheet lying below sand layers is pulled out below a fixed and rigid backstop [e.g., Konstantinovskaya and Malavieille, 2011]. This setup also matches the boundary conditions used in the analytical critical wedge theory [Davis *et al.*, 1983; Dahlen *et al.*,

**Table 1.** Initial Geometrical Parameters

Parameter	Description	Shale Related Simulations	Salt Related Simulations
$H$	Height of the initial setup (m)	5000	3000–6500
$H_s$	Thickness of the overburden (m)	4500	2500, 4500
$H_b$	Thickness of the basal décollement (m)	500	500–2000
$H_m$	Thickness of the intermediate décollement (m)	300 <sup>a</sup>	500 <sup>a</sup>
$L$	Initial length of the model (km)	300 (200 <sup>a</sup> )	300 (200 <sup>a</sup> )
$V_x$	Compression velocity (cm/a)	1	1
$V_z$	Vertical velocity (cm/a)	0	0
$nx$	Number of elements in $x$ direction	900 (600 <sup>a</sup> )	900 (600 <sup>a</sup> )
$nz$	Number of elements in $z$ direction	60	30–75

<sup>a</sup>Values related to multiple décollement setups.

1984]. Numerically, we apply free surface conditions on the top layer and a no-slip boundary at the left side, non-deformable backstop. At the bottom and the right side, a negative constant horizontal velocity ( $V_x =$  compression velocity) and zero vertical velocity ( $V_z = 0$ ) are applied, compressing the model in the horizontal direction. A singularity point is included at the left bottom node, the base of the backstop (Figure 4b). At this point, the code solves the system of equations with the bottom horizontal velocity. The resulting new coordinates of this point are reset afterward to their initial value.

[22] The initial geometric values of the simulations are listed in Table 1. Thicknesses of 2500 and 4500 m of scraped-off rock sequence are implemented for single salt décollement setups only. Variation of basal salt layer thickness (500 m, 1000 m, 2000 m) are applied for both single and multiple décollement simulations.

[23] The characteristic rock parameters for the overburden sequence and the different décollements are listed in Table 2. All simulations contain an identical viscoelastoplastic rock pile representing scraped-off upper crustal levels. Basal and intermediate shale décollements exhibit the same viscosity and shear modulus values as the overlying “rocks,” but have a lower failure criterion with a friction angle of  $5^\circ < \phi_b < 25^\circ$  and no cohesion. The values for  $\phi_b$  in relation to  $\phi = 30^\circ$  stand for the range of existing total taper angles of natural accretionary wedges. (Table 3) Viscosities implemented for basal and intermediate Newtonian salt layers range from  $10^{17}$  to  $10^{20}$  Pa·s. For non-Newtonian salt, a power law coefficient of 5 has been used for a salt temperature of  $50^\circ\text{C}$  [Li *et al.*, 2012] (Table 4).

**Table 2.** Parameters for Rock Sequence and Décollements

Parameter	Description	Rock Sequence	Shale Layers	Salt Layers
$\phi$	Friction angle ( $^\circ$ )	30	5–25	30
$C_0$	Cohesion (MPa)	20	0	20
$\eta$	Viscosity (Pa·s)	1e25	1e25	1e17–1e20
$\rho$	Density ( $\text{kg}/\text{m}^3$ )	2700	2200	2200
$G$	Elastic shear modulus (Pa)	2e9	2e9	2e9
$n$	Power-law coefficient	1	1	1, 5

**Table 3.** Parameters for Simulations With Single (F) and Multiple Frictional (DF) Décollement Layers

Simulation	$\phi_b$ ( $^\circ$ )	$\phi_m$ ( $^\circ$ )	Figure
F1	5	-	5, 6, 9
F2	10	-	4, 5
F3	15	-	5
F4	20	-	5
F5	25	-	5, 6
DF1	5	10	10, 11
DF2	10	10	10
DF3	10	5	10, 11

[24] A diffusional sedimentation process depending on the surface curvature has been implemented to consider surface processes:

$$\frac{\partial h_s}{\partial t} = \kappa \cdot \frac{\partial^2 h_s}{\partial x^2}, \quad (10)$$

where  $\kappa$  is the diffusion constant, and  $h_s$  the surface topography. The equation was solved numerically using the Finite Differences first-order backward diffusion approximation for the top nodes of the model. In all simulations  $\kappa$  has a value of  $10^{-20}$   $\text{m}^2/\text{s}$ . Numerical sedimentation is accomplished by only updating the coordinates at locations where diffusion increased topography.

## 4. Results

[25] We discuss the influence of décollement architecture and rheology on the structural evolution of fold-and-thrust belts. The results are split in simulations with either salt or shale décollement types and with either multiple weak layers or only a single basal décollement. In all presented simulations, frictional shale décollements are displayed with green (basal) and blue (intermediate) colors and viscous salt layers with gray scale (linear viscous) and violet (power law viscous) colors. Beige and brown color bands display the initial horizontal layering of the rock stratigraphy. The color difference is a passive marker for visualization, marking no difference in rock properties. A velocity heterogeneity always occurs at the bottom left singularity point because we employed identical boundary conditions in all simulations. This implies that the first shear band originates from this point in all simulations, independent of salt or shale, single or multiple décollements.

### 4.1. Single Frictional Décollement

[26] Snapshots of a typical simulation with a single frictional (shale) décollement show that deformation starts at the

**Table 4.** Parameters for Simulations With Single (V) and Multiple Linear Viscous (DV) and for Single (P) and Multiple Power-Law Viscous (DP) Décollement Layers

Simulation	$\eta_b$ (Pa·s)	$\eta_m$ (Pa·s)	$H_S$ (m)	$H_b$ (m)	Figure
V1	1e17	-	2500	500	9
V2	1e18	-	2500	500	9
V3	1e19	-	2500	500	9
V4	1e18	-	4500	500	9
V5	1e18	-	4500	1000	9
V6	1e18	-	4500	2000	9
V7	1e19	-	4500	500	10
DV1	5e19	5e19	4500	500	11
DV2	1e19	1e19	4500	1000	11
DV3	1e18	1e18	4500	1000	11
Simulation	$n$	$T$ (°C)	$H_S$ (m)	$H_b$ (m)	Figure
P1	5	50	2500	500	13
P2	5	50	4500	2000	13
DP1	5	50	4500	500	13
DP2	5	50	4500	1000	13

rear of the model and migrates away from there while forming in-sequence, forward verging thrust sheets (Figure 5). The plots below the snapshots show the effective (black) and yield (gray) differential stresses in the lowermost element row. For all snapshots, stresses in the décollement exceed yield stresses  $\sim 40$  km further away from the backstop than the actual deformation front in the overburden sequence. This happens because along the  $\sim 40$  km of décollement failure the hanging wall is not at its yield stress; therefore, the equivalent rock sequence undergoes pure shear. This explanation is supported by the fact that the length of failure at the base, in front of the wedge, decreases with an increasing strength of the basal décollement.

[27] Simulations with a single frictional décollement were investigated with a wide range of yield strengths (Figure 6; simulations F1–F5). Total tapers of the thrust wedges are larger for larger basal friction angles and roughly correlate with the theoretical minimum critical taper angles derived from the critical wedge theory (Figure 2 and plotted lines in Figure 6).

[28] For all simulations with frictional décollement, the frontal thrust is active until the basal yield stress in front of the wedge toe is exceeded. Then, the toe of the wedge jumps by a distance  $L_W$  according to the following equation:

$$L_W = 2 \cdot \frac{H_S}{\tan \theta}, \quad (11)$$

where  $L_W$  depends on the sequence thickness  $H_S$  and the inclination  $\theta$  from horizontal of the shear band defining the new ramp (Figure 7a), which in our numerical simulations initially follows Arthur rather than Coulomb orientations [Kaus, 2010]. The initial inclination  $\theta$  of the shear bands at the wedge toe is independent of the décollement strength (Figure 7) because  $\sigma_1$  is close to horizontal in the undeformed rock pile, in front of the wedge toe. Accordingly, new shear bands are conjugate. However, these shear bands do not necessarily mark the location of the next ramping thrust. This is the case only if the friction angle in the basal décollement is relatively low ( $\phi_b < 10$ ). For larger basal friction angles, the deformation front is more dynamic and constantly generates new shear bands

dipping toward the wedge (Figure 7b). Such shear bands do not necessarily produce recordable offsets and strain rates decrease very fast as long as a new active frontal ramp has not formed.

[29] The orientation of the principal stresses within the wedge produces ramp thrusts that are shallower dipping with increasing basal friction angle (Figure 7b). The largest principal stress  $\sigma_1$  is close to horizontal for compressional wedges with a very weak décollement. For wedges with a higher basal friction angle, i.e., with a larger total taper,  $\sigma_1$  is steeper, raking away from the rear. This is due to a stronger asymmetric gravitational potential in large-tapered wedges. Backthrusts occur predominantly in simulations with  $\phi_b > 10^\circ$  at the rear of the wedge. Backthrusts are steeper than forward verging ramps depending on the direction of the principal stresses (Figure 7b). Our model results (Figure 7) agree with the angles  $\psi_b$  between the horizontal décollement and  $\sigma_1$  predicted by the critical wedge theory [Dahlen, 1984, Figure 2]. Ramp and back thrust dipping angles within the wedge follow Coulomb orientations (Figure 7). This stands in contrast to the initial thrust orientation mentioned above.

[30] Figure 8 shows the distance of the deformation front to the backstop versus time. These plots have been computed at every tenth time step by extracting the  $x$  coordinate of the surface boundary node, which has an elevation difference ( $z$  coordinate) of 5 m to the closest node in  $x$  direction and is furthest away from the backstop. The elevation difference of 5 m implies a slope of  $1.5^\circ$  for an undeformed grid. This value was found to be appropriate for our purpose.

[31] The step-like shape of the graphs for low basal friction angles (Figure 8a) indicates a sudden jump of the deformation front (increase of distance to backstop over a short amount of time). The forward shift of the deformation front in models with high friction angles at the base can be observed in the graphs for higher basal shear resistances ( $\phi_b > 10$ ; Figure 8a). The steps become smaller in space and time and thus increase in numbers. Slightly larger steps every  $\sim 1.8$  Ma indicate the formation of a new frontal ramp with visible offset. The rate of forward migration of the deformation front decreases with increasing basal strength (Figure 8a). For the setup with  $\phi_b = 5^\circ$  the wedge toe migrates at a rate  $\sim 2$  cm/a over the first 3 Ma and then reaches an average rate of  $\sim 1$  cm/a for the rest of the simulation time. With  $\phi_b = 25^\circ$ , the frontal thrust migrates away from the rear at  $\sim 1$  cm/a over the first 2 Ma and  $\sim 0.5$  cm/a for the next 10 Ma (Figure 8a). The fact that the distance from the toe to the backstop decreases during the activity of a single frontal thrust, i.e., the slopes of the graphs are negative, indicates internal, horizontal shortening of the wedge. This internal strain is not related to the frontal thrust zone.

#### 4.2. Single Linear Viscous Décollement

[32] As stated earlier, the shear resistance to sliding along viscous (salt) décollements is influenced by more factors than along a frictional base. For sake of clarity, all presented results were obtained with a shortening velocity of 1 cm/a. Simulations with higher rate were performed as well, but the influence of this rate on the shear stress in the décollement is minor compared to uncertainties in the values of effective viscosity (see equation (3) and Table 2).

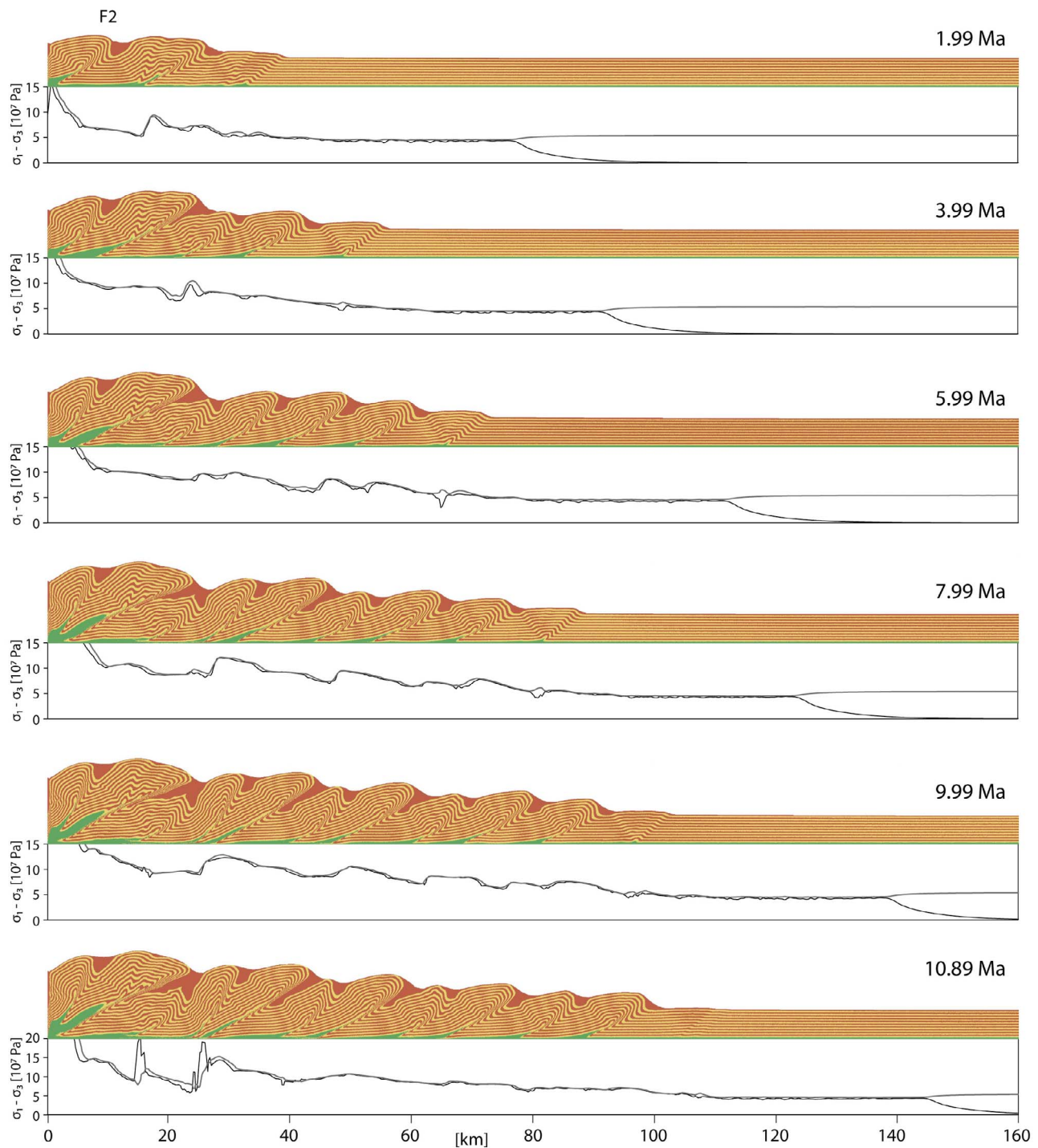


**Figure 5.** Temporal evolution of fold-and-thrust belt (beige and brown,  $\varphi = 30^\circ$ ) with a frictional décollement (green,  $\varphi_b = 10^\circ$ ). Thrust wedge grows horizontally by in-sequence thrusting and vertically by reactivating thrusts within the wedge. Most of the horizontal shortening is accommodated by the active frontal thrust. Plots show the differential stress (black line) and the differential yield stress (gray line) in the lowest element row (no vertical exaggeration).

[33] Shear stresses in salt décollements follow equation (3). This implies that shear stresses in the salt increase with increasing viscosity and decreasing thickness. It also results in a decrease of velocity difference  $\Delta u$  between the bottom and the top of the salt. Since the velocity at the salt bottom is

constant (compression velocity), the decrease of  $\Delta u$  results in a drag of upper crustal material toward the backstop. If the resulting shear stresses are low enough (critical taper  $\sim 1^\circ$ ;  $<2.5$  MPa if  $H_S = 2.5$  km,  $<7.5$  MPa if  $H_S = 4.5$  km; Figure 3),  $\Delta u$  can reach the value of the shortening rate and

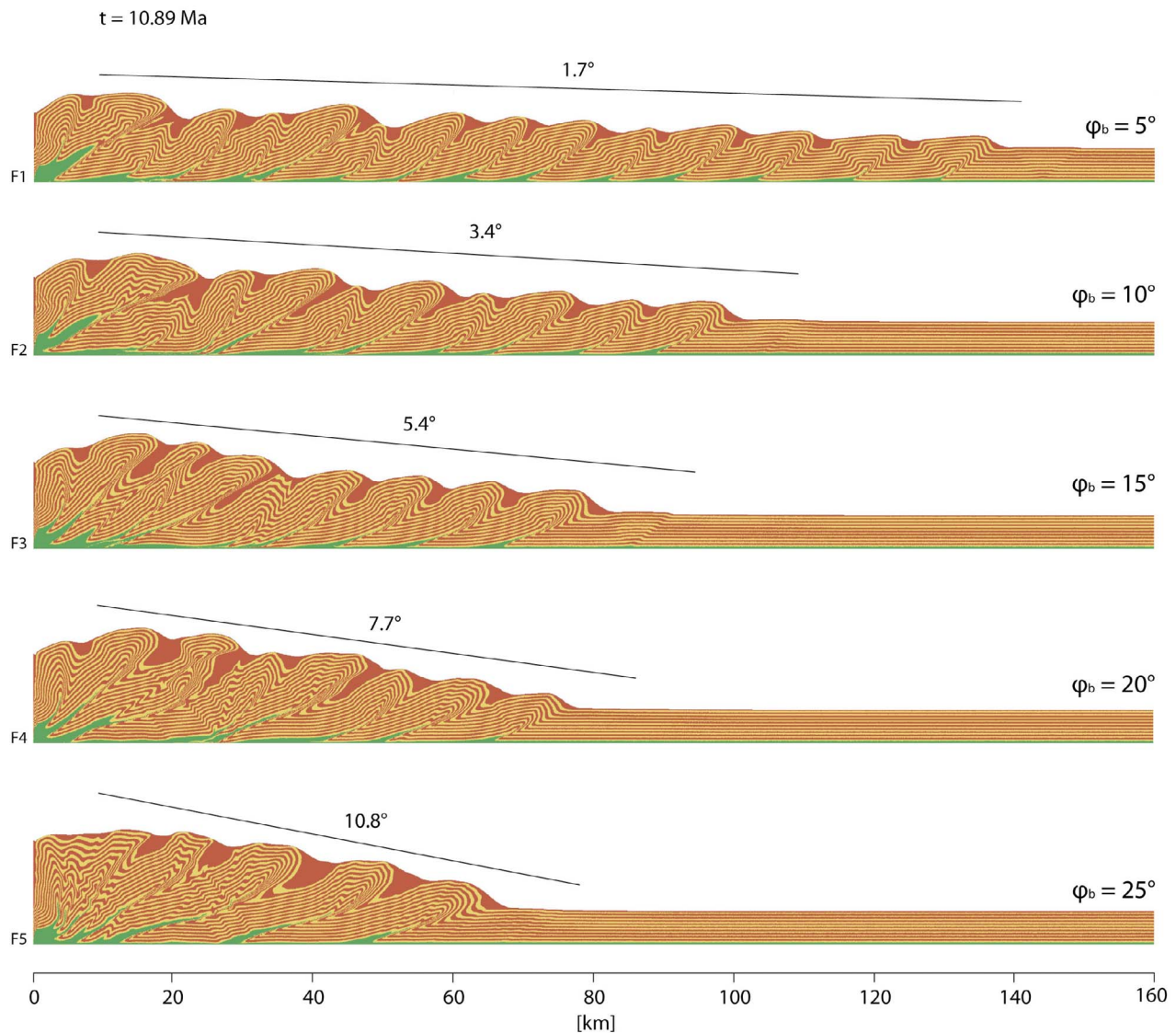


**Figure 6.** Wedges of layered sequences (beige and brown) over frictional décollement (green) with different basal frictional strengths ( $\phi_b$ : 5, 10, 15, 20, 25°) after 10.89 Ma. Friction angle of the pile:  $\phi = 30^\circ$ . Increasing the basal friction angles decreases the dip angles of forward verging ramps and makes thrust sheets longer. Straight lines indicate analytically derived surface tapers from the critical wedge theory (Figure 2) (no vertical exaggeration).

there is no drag of the rock sequence toward the backstop. To better understand the consequences of this, simulations with identical shortening rates and sediment and salt thicknesses have been performed. Different shear stresses were achieved with different viscosity values. For low salt viscosities ( $\leq 10^{18}$  Pa·s), i.e., low basal shear stresses, critical taper angles of  $\sim 0.2^\circ$  lead to a distributed deformation away from the backstop and eventually to folding and thrusting spatially unrelated to any previously developed structure. Symmetrical box folds or conjugate thrusts develop because the main principal stress acts horizontally. For simulations with a salt layer thickness of 500 m, a rock pile thickness of 2.5 km and a shortening rate of 1 cm/a, a viscosity  $< 1 \cdot 10^{19}$  Pa·s is required to yield the formation of single-standing box folds (Figure 9a). Higher basal viscosity causes a drag of overburden toward the backstop due to lower shear

strain rate within the décollement, resulting in wedge-shaped fold-and-thrust belts (Figure 9a). For models with a rock thickness of 4.5 km, migration rates of the deformation front are  $\sim 0.4$ –5 cm/a (Figure 8b). The thickness of a basal salt layer influences the basal shear stress proportionally (see equation (3)). Furthermore, it is also influencing the deformation mechanisms of thrusting and folding. The overburden can sag more easily on a thicker viscous basal layer and, therefore, thrusts may have larger offsets and more asymmetry (Figure 9b).

[34] Frictional layers fail when shear stresses exceed their yield strength. The wedge slides on the failing décollement up to the active frontal thrust. In the very front of it, the rock sequence undergoes pure shear over the length where the décollement is at its yield stress (Figure 5). Therefore, stresses can disperse into the wedge as far as pure shear appears

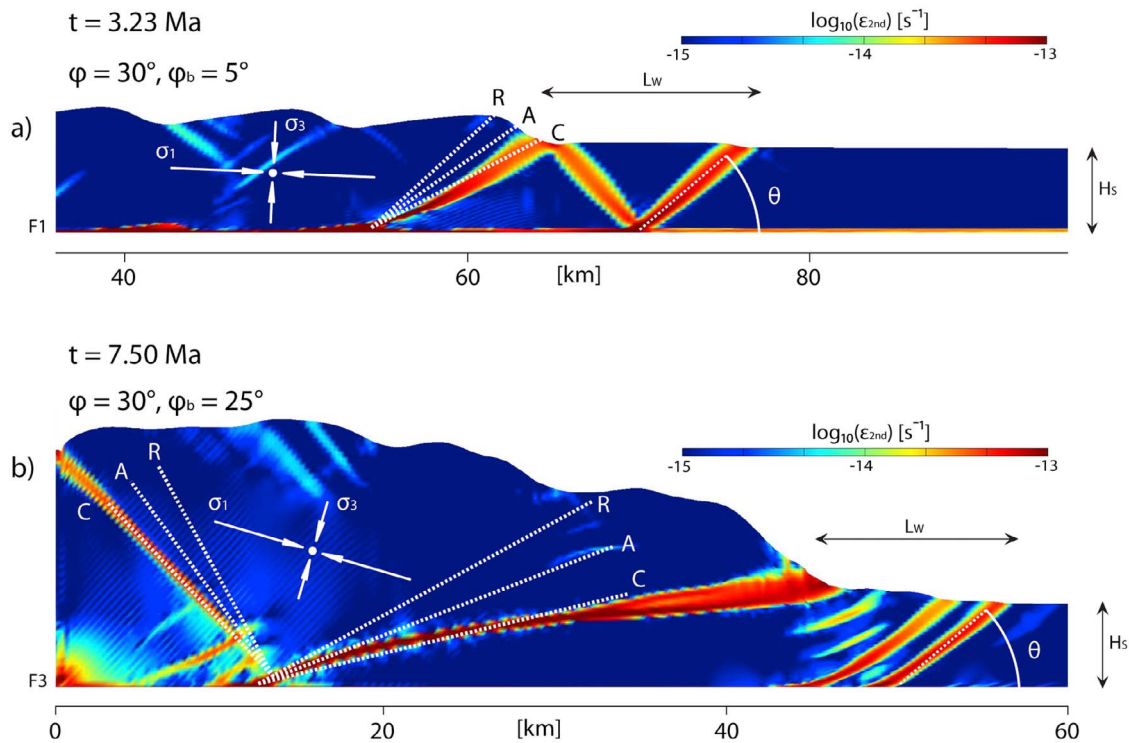


**Figure 7.** Second invariant of the strain rate tensor. Jump of deformation in a frictional wedge with basal friction angles  $\phi_b$  of (a)  $5^\circ$  and (b)  $25^\circ$ . Dip angles of the developing shear bands in the undeformed rock pile are identical in Figures 7a and 7b. Jump of deformation  $L_w$  (equation (11) in text) depends on the sequence thickness  $H_s$  and the angle  $\theta$  between the shear band and the décollements. Stress orientations (converging white arrows) have analytically derived values according to the critical wedge theory [Dahlen, 1984]. Dotted lines indicate Coulomb (C), Arthur (A), and Roscoe (R) angles derived from the theoretical stress field (no vertical exaggeration).

(Figure 10). In contrast, a low-viscosity salt décollement cannot fail since there is no yield criterion. This leads to increased strain rates even at low stresses. High strain rates in basal viscous layers propagate long distances away from

the deformation front, leading to high differential stresses in the layered sequence in front of the wedge, i.e., that part which is not yet incorporated in the fold-and-thrust belt (Figure 10b).

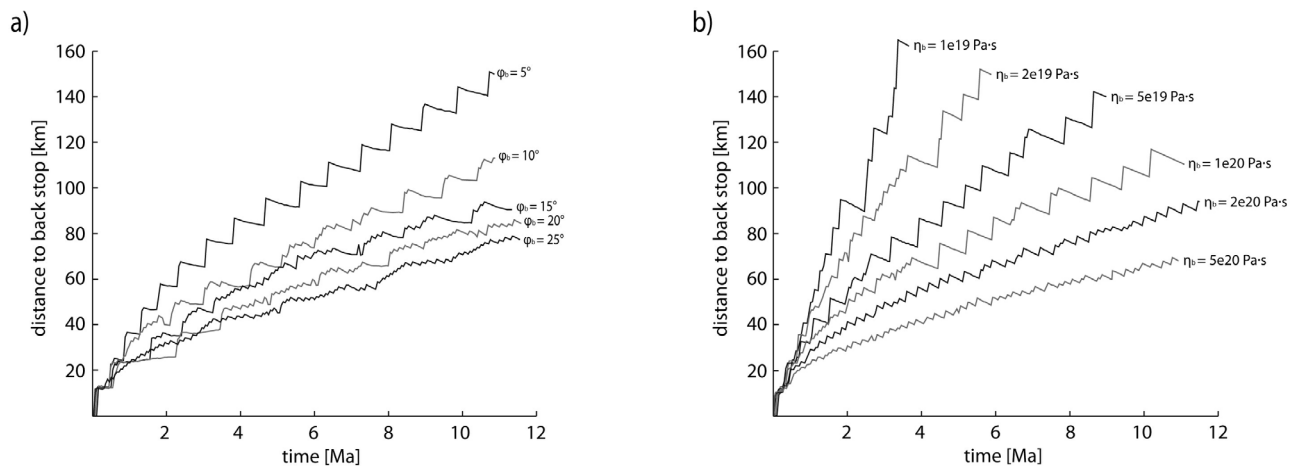


**Figure 8.** Horizontal evolution of fold-and-thrust belts overlying (a) single shale and (b) salt décollements with different strengths. Average gradient of kinked lines indicate rate of migration of the deformation front away from the rear. In Figure 8a, abrupt jumps in deformation front:  $\phi_b = 5^\circ$ . If  $\phi_b > 5^\circ$ : shift of the deformation front through time. In Figure 8b, decreasing salt viscosity results in a faster horizontal growth of the wedge. Wide fold belts with single-standing structures:  $\eta_b < 1e19$  Pa.s.

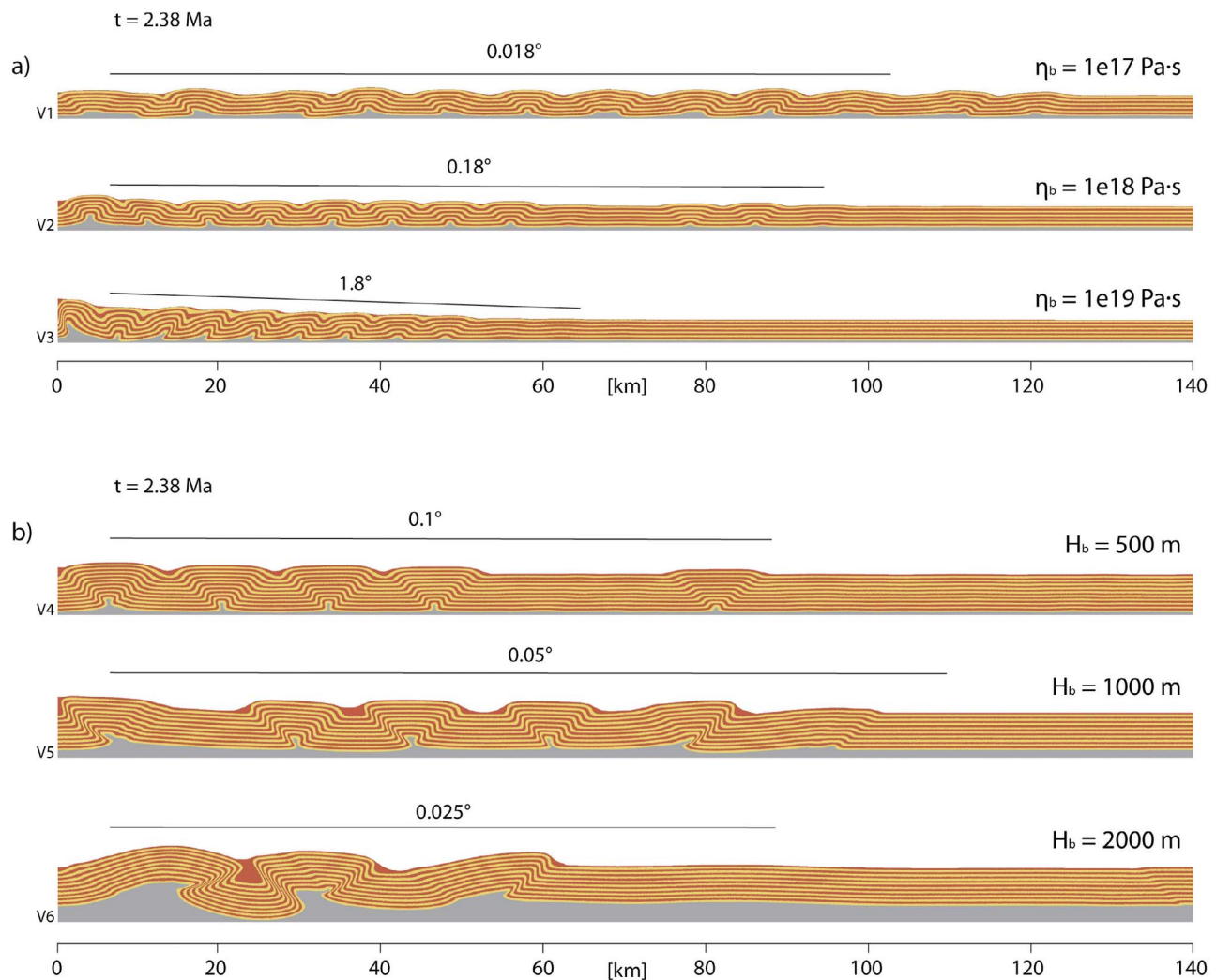


**Figure 9.** Comparison of fold-and-thrust belts overlying salt décollements after 2.38 Ma. Straight lines indicate analytically derived surface tapers from the critical wedge theory (Figure 3). (a) Effect of salt viscosity ( $\eta_b$ ). Values for each simulation in Table 4. Folding is favored:  $\eta_b = 1e^{17}$ . Very wide fold belt. Box folding of sequence with the appearance of proximal single standing box folds:  $\eta_b = 1e^{18}$  Pa·s. Drag of rock sequence toward backstop and forward verging thrusting:  $\eta_b = 1e^{19}$  Pa·s. (b) Variation of salt décollement thickness ( $H_b$ ). Development of single-standing box folds and low anticline amplitudes:  $H_b = 500$  m. Thrust initiation with no preferred vergence:  $H_b = 1000$  m. Structures are not necessarily attached to each other. Thrusts with no preferred vergence and larger offsets:  $H_b = 2000$  m. Increase of wavelength (no vertical exaggeration).

#### 4.3. Two Frictional Décollements

[35] Adding a frictional (shale) décollement layer within the wedge sequence yields important structural differences with simulations with a single basal décollement (Figure 11a). The depth of the second weak layer has been conveniently chosen for all simulations to be at two thirds from the basal décollement. This is consistent with the fact that weak layers in frictional fold-and-thrust belts are commonly made of overpressured shale, which needs a certain depth of burial so that the water pressure is sufficient to reach the failure criterion [Platt, 1990].

[36] Fold-and-thrust belts with two frictional décollements grow sequentially like simulations with a single basal décollement (Figure 5). However, instead of thrust sheets

and fault planes normally reaching from the surface down to the single décollement, shear bands and folds are interrupted downward by the intermediate weak décollement and develop a wedge-scale duplex structure.

[37] Yet, the cross-sectional taper of the fold-and-thrust belt depends on the strength of the deepest active décollement. This means that failure of the basal décollement results in deformation of the whole layered sequence independent of the stress state within the weak intermediate layer. Deformation involves interplay between structures above and below the weak intermediate layer. Consequently, a failing intermediate layer and a stable base within the same vertical profile lead to underthrusting (tectonic underplating) of material below the deforming upper sequence (Figure 11a, simulation DF3).

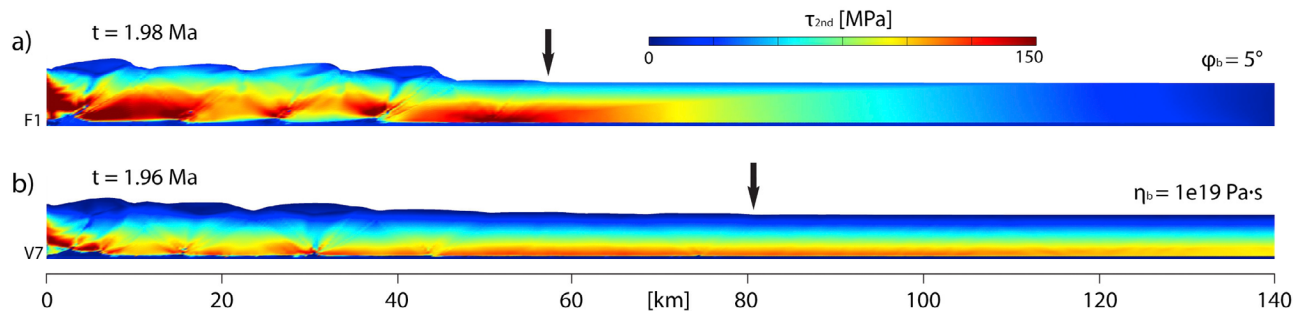


**Figure 10.** Second invariant of the deviatoric stress tensor. Black arrows point to the location of the deformation front. (a) Wedge with a frictional décollement ( $\phi_b = 5^\circ$ ). In front of the wedge toe, the basal layer is not at the yield stress. Therefore, no failure occurs along the décollement and stresses do not disperse far into the undeformed layered sequence. (b) Wedge over a salt décollement ( $\eta_b = 1e^{19} \text{ Pa}\cdot\text{s}$ ). Initial low viscosity results in high strain rates in the viscous layer. Stresses are dispersed throughout the layered sequence (no vertical exaggeration).

[38] Three simulations with different relationships between the basal and the within-sequence décollements are discussed (Figure 11a). If the basal décollement is weaker than the intermediate one ( $\phi_b < \phi_m$ ), the overall cross-sectional taper is controlled by the strength of the basal weak layer (simulation DF1). The theoretical minimum critical taper angle of  $1.7^\circ$  is consistent with the simulation result (Figure 11a, simulation DF1). Two structural wavelengths develop according to equation (11): (1) a short wavelength restricted to the uppermost pile, which is a function of the depth of the upper décollement and (2) a broad wavelength, throughout the wedge, which depends on the depth of the basal décollement. The long-wavelength structures initially arise in the upper part of the rock pile, with fault propagation folds (Figure 11a, simulation DF1) evolving into ramp faults affecting the whole pile (Figure 12a). The fast growth of upper partial fault propagation folds at the toe of the wedge locally overcomes the critical taper related to the intermediate décollement and controls the short-wavelength structures in the upper pile. In contrast, the forward jump of a ramp crosscutting the whole sequence depends on the critical taper of the complete wedge, which grows much slower. Therefore, a relatively long wavelength in relation to the complete pile is produced.

[39] The same strength for the basal and the intermediate décollements ( $\phi_b = \phi_m$ ), intensifies tectonic underplating below the upper décollement (simulation DF2). New frontal thrusts, soling to the base, occur at regular intervals (Figure 11a, simulation DF2). The theoretical minimum taper angle predicted by analytical solutions for a frictional strength  $\phi_b = \phi_m = 10^\circ$  and an internal friction angle  $\phi = 30$  is in this case  $3.4^\circ$  (Figure 2). The numerical models show a slightly steeper angle ( $5^\circ$ ). This very small discrepancy could be due to underplating and surface uplift of the rear part by antiformal stacking (Figure 11a, simulation DF2). Wavelengths on the surface depend on the thickness of the upper sequence after equation (11). Ramping of the lower sequence occurs with no preferred distance between thrusts.

[40] Simulations in which the intermediate décollement is weaker than the basal décollement ( $\phi_b > \phi_m$ ) are characterized by an unambiguous decoupling between the upper and lower parts of the wedge (Figure 11a, simulation DF3). As previously discussed, the taper angle increases with increasing basal strength while the forward migration rate of the

frontal thrust decreases (Figure 6). Accordingly, the critical taper angle related to the intermediate décollement is smaller than that resulting from the basal décollement. Therefore, the deformation front of the upper sequence migrates faster than in the lower part. This leads to deformation propagating in the upper sequence without affecting the underthrust lower part. The ramp spacing depends on the initial sequence thickness according to equation (11), i.e., only the thickness of the upper sequence. The surface slope of the distal part of the model agrees with the expected minimum critical taper ( $1.7^\circ$ ), whereas the surface of the rear part, which is also influenced by underplating, is steeper ( $6\text{--}7^\circ$ ) than the theoretical value ( $3.4^\circ$ ). This difference results from strong underplating and the influence of the weak intermediate layer on the stress state of these underlying, underplating rocks.

[41] In summary, the style and location of deformation in wedges with several frictional décollements vary strongly. In a fold-and-thrust belt with a weak intermediate layer, yet stronger than the basal décollement, critical stresses and therefore deformation occur predominantly at the front of the taper, with ramps climbing from the décollement to the surface (Figure 12a). If an intermediate layer is weaker than the basal décollement, a décollement takes place along this layer, preventing high stresses in the lower rock sequence (Figure 12b). This allows underthrusting. Deformation mainly acts in the upper part, at the wedge toe, whereas underplating and eventually antiformal stacks occur in the lower part, near the rear of the wedge (Figure 12b).

#### 4.4. Two Linear Viscous Décollements

[42] In simulations with viscous (salt) décollements, strain rates increase within these layers compared to the surrounding layers, even at low stresses. For simplicity, we focus on cases in which the viscosity in the basal and in the intermediate décollement is the same. This stands in contrast to simulations with multiple frictional décollements, where the relative strength of the weak layers with respect to each other is the factor determining the deformation style of an evolving fold-and-thrust belt.

[43] Three simulations with the basal shear stress decreasing by a factor of ten are presented (Figure 11b). The maximum basal shear stress is adjusted by means of the layer thickness and viscosity (see equation (3)). Simulations

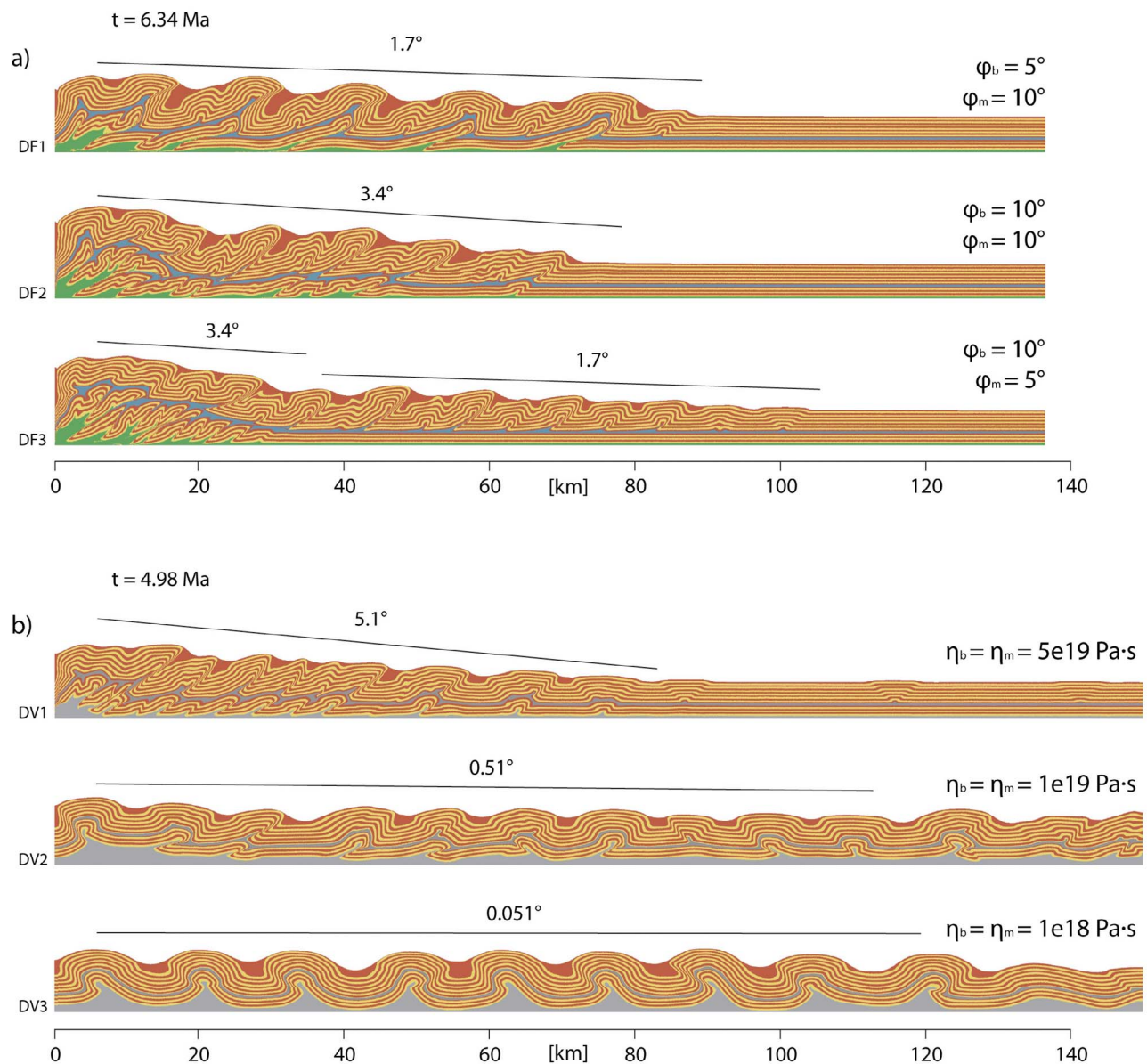


**Figure 11.** Simulations with multiple décollements. (a) Basal and intermediate décollements consist of shale (green and blue) and are shown after 6.34 Ma. Straight lines indicate analytically derived surface tapers from the critical wedge theory. Simulation DF1: Intermediate décollement is stronger than basal one. The total wedge taper depends on frictional strength of basal décollement. Simulation DF2: Intermediate and basal décollement have the same strength. Simulation DF3: Basal décollement is stronger than intermediate one. Underplating leads to antiformal stacking at the rear. Short-wavelength imbrication appears at the toe in the rock pile. (b) Simulations with two salt layers (gray scale) compressed during 4.98 Ma. Simulation DV1: High salt viscosity produces drag toward the backstop. Simulation DV2: Fault propagation folds with no preferred vergence. Very low surface taper. Simulation DV3: Low salt viscosity and increased salt thickness result in open folds with wavelengths comparable to Zagros folded belt [Mouthereau *et al.*, 2007a, 2007b; Yamato *et al.*, 2011] (no vertical exaggeration).

with two viscous weak layers grow sequentially with the same rate of frontal migration as the equivalent single décollement simulations. In two-décollement simulations with décollement viscosity of  $5 \cdot 10^{19} \text{ Pa}\cdot\text{s}$  and a basal salt thickness of 500 m, the rock sequence is dragged toward the backstop and builds a wedge-shaped taper (Figure 11b, simulation DV1). The presence of an intermediate viscous

layer concentrates high strain rates between the lower and the upper wedge pile, where faulting is the dominant mode of deformation. Forward verging imbrication independently evolves in the lower and the upper parts. Thrust sheet dimensions depend on the respective thicknesses. Folding occurs at the toe of the wedge in form of long-wavelength fault propagation folds in the upper part and in form of

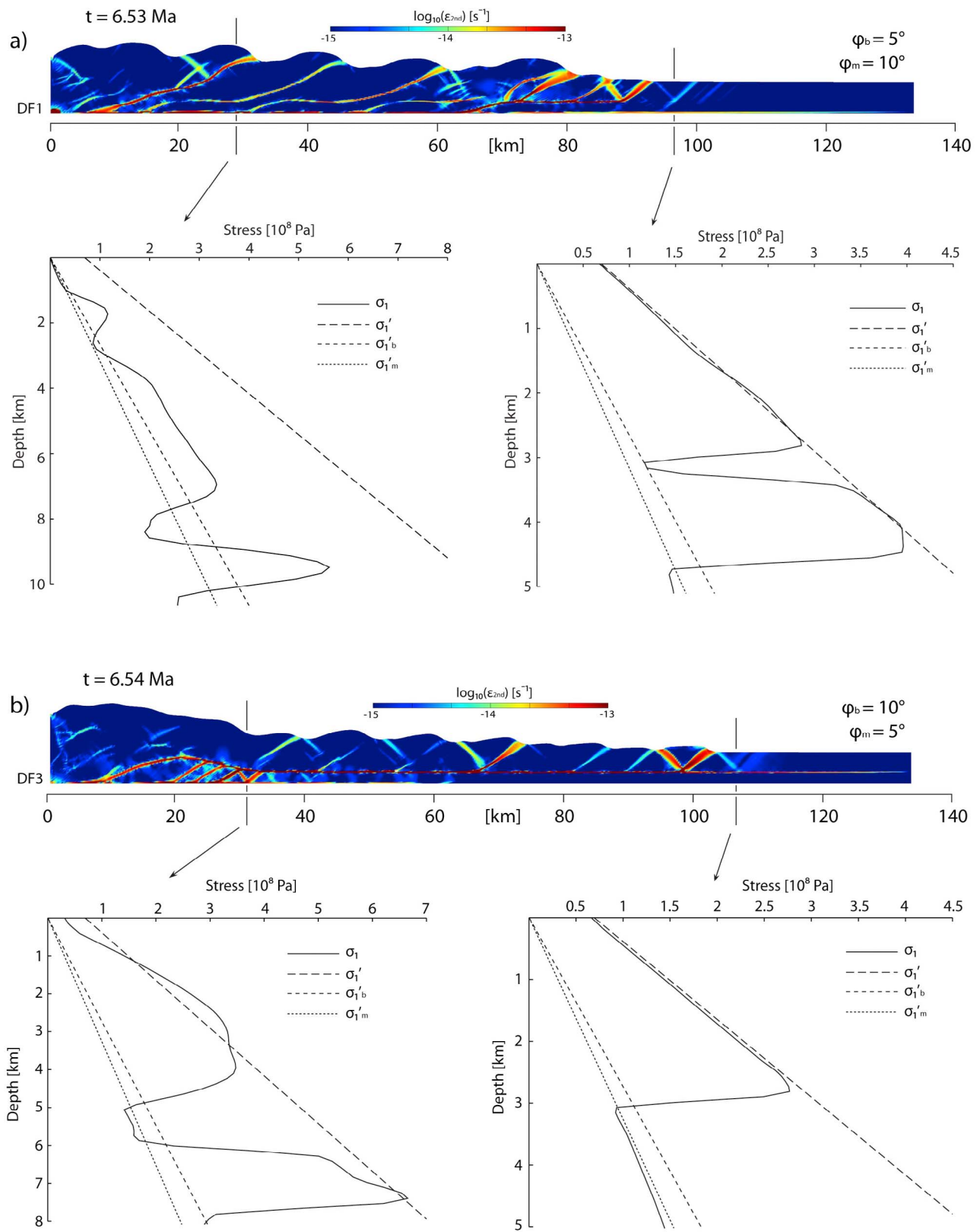


**Figure 12.** Second invariants of the strain rate tensor for simulations with two frictional décollements. (a) The intermediate décollement is stronger ( $\phi_b = 10^\circ$ ) than the basal décollement ( $\phi_b = 5^\circ$ ). (b) Intermediate décollement is weaker ( $\phi_b = 5^\circ$ ) than the basal décollement ( $\phi_b = 10^\circ$ ). Stress profiles of distal and proximal parts for both cases. Empirical  $\sigma_1$  (full line); theoretical main principal stresses  $\sigma'_1$  needed to fail the layered rock sequence and the weak layers (dashed lines) (no vertical exaggeration).

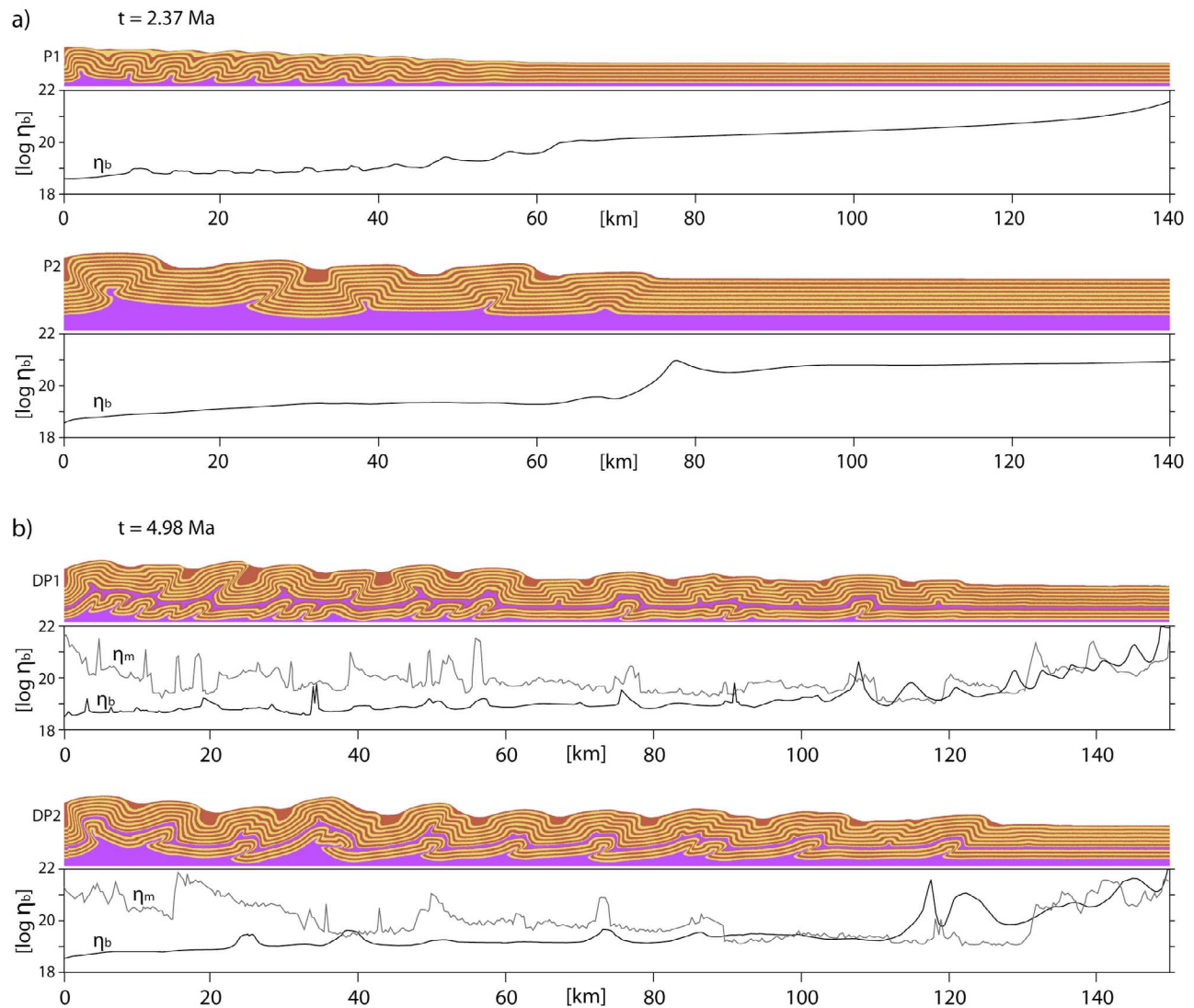


**Figure 13.** Simulations with nonlinear viscous salt décollements. (a) Single basal décollement. (b) Basal and intermediate décollements. Plots show the effective viscosity of the lowermost element row in the basal salt (black) and the lowest viscosity in every element column in the intermediate décollement (gray). See Table 4 for initial geometry and rheological parameters.

isolated box folds  $\sim 30$  km in front of the toe in the upper part.

[44] If the salt viscosity is divided by five and the salt thickness is doubled, folding becomes more important (Figure 11b, simulation DV2). The lower part of the wedge is mainly deformed by thrusting, backthrusts and forward verging ramps appearing equally. The upper part shows three types of structures: (1) long-wavelength (10 km) fault propagation folds, (2) thrust ramps that reach down to the basal décollement, and (3) ramps contained within the upper wedge sequence (at a width of  $\sim 90$  km).

[45] Decreasing the salt viscosity tenfold leads to a fold-dominated structural pattern (Figure 11b, simulation DV3). The folds are open and show a regular wavelength of  $\sim 15$  km. Although folding dominates, thrusting still accommodates some shortening. Fault planes appear as forward

verging ramps and as backthrusts and cut through the complete rock sequence (Figure 11, simulation DV3). The weak material has a high flow potential and is able to fill the hinge of a growing anticline. The effect of an additional intermediate décollement on the deformation mode is best demonstrated by comparing single décollement with two-décollement simulations. Setups without an intermediate décollement show faulting as dominant deformation mode (Figure 9b, simulation V2), whereas an identical setup with an intermediate décollement is fold dominated (Figure 11b, simulation DF3). Physically, this reflects the fact that the folding growth rate of a multilayer sequence is larger than that of a single layer [Schmid and Podladchikov, 2006; Yamato et al., 2011]. If the overburden had a purely viscous rheology, the single layer case would deform by pure-shear thickening. As it is brittle in our simulations, faulting dominates. The case with an

additional décollement layer, however, produces folds in a sufficiently rapid manner to install folding as the dominant deformation mode.

#### 4.5. Simulations With Nonlinear Viscous Décollements

[46] *Urai et al.* [2008] argued that the deformation mechanism for coarse grained salt is defined by dislocation creep with a power law coefficient of  $n \approx 5$ . Accepting this argument, simulations with power law viscous décollements were carried out using the rheology of *Li et al.* [2012], which describes the relationship between differential stress and strain rate. The initial geometry and defined parameters for the corresponding simulations are summarized in Table 4. Throughout basal décollements, a constant temperature of 50°C (following *Li et al.* [2012]) is implemented for every setup.

[47] Figure 13a shows two simulations with a single nonlinear viscous ( $n = 5$ ) basal décollement (simulation P1, P2). The plots below the horizontally compressed stratigraphy illustrate the effective viscosity in the bottom element row at the same time step. Simulation P1 has the same initial geometry as simulations in Figure 8a. Structurally, it is comparable with simulation V3, where the basal décollement has a viscosity of  $10^{19}$  Pa·s. This is featured by the effective viscosity plot of simulation P1 in Figure 13a, which shows similar values as V3 below the deformed sequence (0–60 km). The drag of overburden material for simulations with a linear viscous basal décollement is not as effective as for nonlinear cases, since the effective viscosity drops at higher stresses. Nevertheless, a wedge-shaped fold-and-thrust belt evolves with forward vergent thrusts (Figure 13a, simulation P1). Simulation P2 has an identical geometric setup as simulation V6 (Figure 8b). The resulting effective viscosities for the bottom element row of simulation P2 are rather higher than the constant viscosity used in simulation V6. Accordingly, the wavelength of the deformation pattern is smaller, but forward verging and backward verging thrusts tend to develop equally (Figure 13, simulation P2).

[48] Figure 13b shows two simulations with multiple nonlinear viscous ( $n = 5$ ) décollements (simulation DP1, DP2) with the related effective viscosity plots below. Besides the viscosity of the lowest element row, the effective viscosity of the intermediate décollement layer is plotted. This has been done by taking the lowest values for viscosity of the intermediate layer for every element column. Simulation DP1 and DP2 are geometrically identical to simulations DV1 and DV2, respectively (Figure 11b). Structurally, they resemble to linear viscous simulations with a décollement viscosity of  $10^{19}$  Pa·s (Figure 11b, simulation DV2). The lower structural level of simulation DP1 forms forward verging fault-bend anticlines. The upper level shows thrusts merging with lower-level ramps and detachment faults without any connection to the lower part. Simulation DP2 has a thicker basal décollement. The ramp spacing in the lower level is consistently larger than in simulation DP1. The upper structural level is predominantly deformed by fault propagation folds cored by the lower ramps (Figure 13b).

#### 4.6. Limitations of the Model

[49] The numerical models presented in this study are very simplified. They concern a horizontally layered sedimentary

pile pushed over a rigid “plate” by a rigid, perfectly vertical backstop. The advantage of this simplified setup is the possibility to compare results with existing analog models, which generally use sand boxes [e.g., *Konstantinovskaya and Malavieille*, 2011]. Furthermore, the simplified setup yields results that can be explained by analytical solutions such as the critical wedge theory, which uses similar geometrical boundary conditions [*Davis et al.*, 1983; *Dahlen et al.*, 1984]. The chosen geometrical simplifications make it impossible to investigate several important factors known in natural fold-and-thrust belts, for example the influence of basement deformation, although thin-skinned and thick-skinned tectonics may coexist (e.g., *Zagros* [*Mouthereau et al.*, 2007b]). Also, the initially undeformed rock pile of the models neglects effects of inherited fault systems (e.g., *Pyrenees* [*Tavani and Munoz*, 2012]). Furthermore, the overburden is set as an isotropic viscosity; the models are therefore unable to address layer parallel slip as reported in turbidites. *Yamato et al.* [2011] investigated the effect of flexural slip by implementing 100 to 200 m thick weak layers. However, the resolution of their and our simulations cannot integrate weak horizons on the centimeters scale of turbidite layers. Numerical models with an anisotropic viscosity are in principle capable of simulating this effect. This was previously shown to increase folding growth rates and produced chevron folds [*Kocher et al.*, 2006].

[50] In this study, imbricate shear bands begin to develop as conjugate thrusts and backthrusts bifurcating from a point in the décollements layer. Out of sequence backthrusts additionally appear in the rear to maintain the critical taper. Although backthrusting is known in natural fold-and-thrust belts, it is less common at the wedge toe than models suggest. This discrepancy may be explained by the homogeneity of the modeled sedimentary pile. Yet, the frontal shear bands of models do not accumulate much strain, and we conjecture that they would be unnoticeable in the field.

## 5. Discussion

[51] The results demonstrate that the rheology of the basal décollement and the presence of weak intermediate layers in the compressed rock pile play key roles in the evolution of a fold-and-thrust belt. Comparing the rheology of shale and salt décollements explains the structural differences of fold-and-thrust belts overlying either of these. If the décollement takes place along overpressured shale, it follows a frictional failure criterion and propagates when stresses overcome the yield stress. If a fold-and-thrust belt is soled by a viscous salt layer, its structural evolution depends on the shear resistance of this layer.

[52] Frictional fold-and-thrust belts grow horizontally in sequence, independent of the strength of the décollement (Figure 5). The resulting total taper angle (Figure 6) and stress fields (Figure 7) are both consistent with the critical wedge theory. The stable frictional wedge is sliding along a basal décollement and accommodates shortening on an active frontal ramp in front of which the décollement does not extend. Therefore, differential stresses cannot build up further away in front of this frontal thrust (Figure 10a).

[53] Fold-and-thrust belts related to salt décollements can develop a wedge-like shape if shear stresses are high; then material is dragged toward the backstop (Figure 9a,

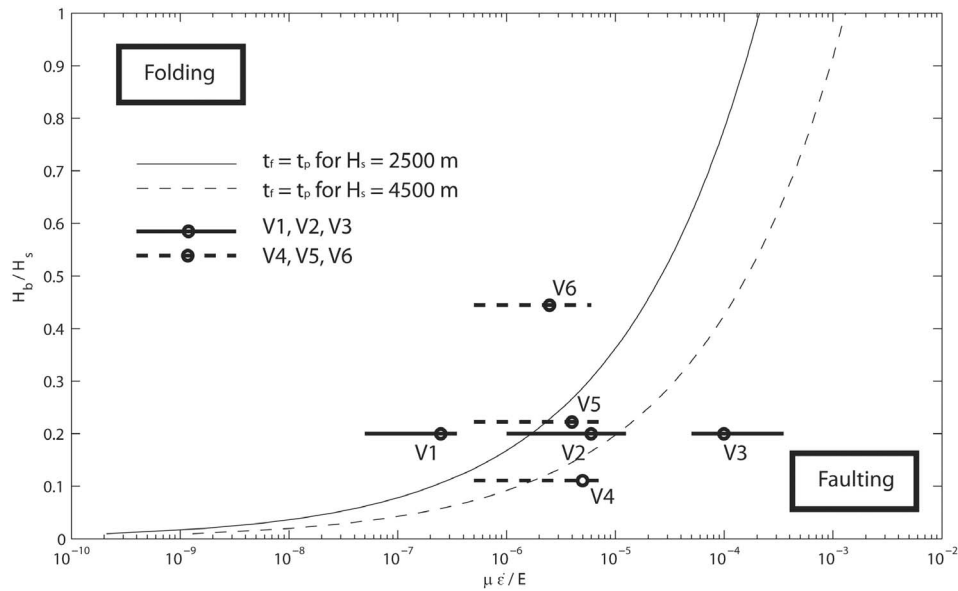


**Figure 14.** Domains of folding/faulting depending on the décollement/overburden ratio and the normalized viscosity by equalizing equations (12) and (13) for overburden thickness of 2500 m (solid line) and 4500 m (dashed line). Thick line segments represent the range of nondimensional values from numerical simulations V1–V3 (solid line) and V4–V5 (dashed line). Circles are projected horizontal axis values for the dominant strain rate of labeled simulations.

simulation V3). Related models exhibit a frontal ramp. Internally, the wedge is constantly compressed as the drag continues because no basal failure occurs. This stands in contrast to frictional décollements, which are at failure. Like this, salt décollements can distribute high strain rates far from the backstop and generate high stresses over a large horizontal distance (Figure 10b). This leads to the development of wide fold-and-thrust belts with little finite shortening, e.g., the Zagros folded belt.

### 5.1. Folding Versus Faulting Analysis for Viscous Décollement Simulations

[54] *Simpson* [2009] provided an analytical solution for whether a horizontally compressed elastic rock sequence overlying a viscous substratum is deformed by folding or faulting. In order to achieve this solution, the time required for fast fold amplification  $t_f$  is compared with the time needed to fault the rock sequence  $t_p$ .

[55] The equation for the folding time  $t_f$  is derived from the maximum growth rate analysis and the equation for the time required to produce an amplitude due to folding.

$$t_f = \frac{9}{16} \frac{\eta_b(1-\nu^2)H_s^3 \ln A}{E\varepsilon^3(1+\nu)^3 H_b^3}, \quad (12)$$

where  $A$  is the amplitude factor (e.g.,  $A = 1000$  for explosive folding [*Biot*, 1961]),  $\nu$  is the Poisson ratio,  $E$  is Young's Modulus,  $\varepsilon$  is strain,  $\eta_b$  is the décollement viscosity,  $H_b$  is the décollement thickness and  $H_s$  the overburden thickness.

[56] The plastic time  $t_p$  is calculated by setting the equation for horizontal elastic stress against horizontal stress needed to build up the Mohr-Coulomb envelope everywhere

in the rock sequence. Then this equation is solved for strain and divided by strain rate

$$t_p = \frac{(1+\nu)(2\nu-1-\sin\phi)\rho g H_s}{\dot{\varepsilon} E(\sin\phi-1)} + \frac{\cos\phi(1+\nu)(2C_0\nu-2C_0)}{\dot{\varepsilon} E(\sin\phi-1)}, \quad (13)$$

where  $\dot{\varepsilon}$  is strain rate. At variance to *Simpson* [2009], the maximum lithostatic pressure is calculated from the thickness of the wedge sequence only instead of the total model thickness. This is due to the fact that the décollement is not behaving plastic but purely viscous.

[57] If  $t_f < t_p$ , fast amplification engenders folding before stresses are at the yield. For  $t_f > t_p$ , the base of the overburden is at failure before an amplitude required for folding has evolved. The case  $t_f = t_p$  designates the boundary between folding and faulting deformation modes. In Figure 14, similar to Figure 12 in *Simpson* [2009], this boundary is shown for two cases ( $H_s = 2500$  m and  $H_s = 4500$  m) as a function of the ratio of the décollement thickness  $H_b$  and the rock sequence thickness  $H_s$  and the normalized viscosity of the décollement. Thick horizontal lines correspond to simulations V1–V3 (full) and V4–V5 (dashed) and illustrate the normalized viscosity using the range of horizontal strain rates observed at the décollement/overburden interface from the numerical results (Figure 14).

[58] The folding versus faulting analysis indicates that folding dominates deformation in simulations V1, V5, and V6. The range of values for normalized viscosity of V2 and V4 trespasses the folding / faulting boundary and simulation V3 plots in the area, where faulting is dominant. For

simulations V1–V3, the change from folding to faulting with increasing décollement viscosity can be observed in Figure 9a. The structural pattern of simulation V2 can be compared with that of simulation V4 (Figure 9), both plotting on the boundary of faulting versus folding (Figure 14). The most controversial cases are simulations V5 and V6, which analytically yield folding as the dominant deformation mode (Figure 14), although numerical simulations illustrate that faulting takes place during shortening (Figure 9b). We conjecture that this anomaly is a result of the fact that our setup implies a velocity bottom boundary condition, whereas the amplification theory is rather applicable to free-slip condition.

## 5.2. Comparison to Natural Fold-and-Thrust Belts

[59] Results indicate that structural styles of fold-and-thrust belts vary according to the type and strength of the main décollement. The occurrence of additional décollements within the thin-skinned rock sequence also influences the structural evolution. Now, several examples of natural fold-and-thrust belts are compared to our modeling results to illustrate the mechanics of their evolution.

[60] The Hikurangi subduction margin, NE New Zealand (Figure 1a), exhibits a thrust imbricated accretionary wedge, up to 150 km wide [Lewis and Pettinga, 1993], and a taper of  $\sim 4^\circ$  [Barnes et al., 2010]. Barnes et al. [2010] characterized the ancient décollement zone as a sheared matrix of mudstones from the upper plate containing basalt and chert blocks from the oceanic lower plate. This indicates that the basal décollement is close to the bottom of the incoming sedimentary sequence. The redrawn seismic section of this accretionary wedge (Figure 1a) shows that there is no major intermediate décollement within the deformed sedimentary sequence and thrust ramps merge into the basal décollement. Imbricated thrusts are preferentially verging toward the front, in the SE (Figure 1a). Barnes et al. [2010] mention an extensive zone of protothrusts beyond the principal deformation front. Such protothrusts locally appear as conjugate systems and usually have an offset of few tens of meters with dips of  $40 \pm 5^\circ$ . These features are consistent with simulations performed with a single frictional décollement (Figure 6). The taper of  $\sim 4^\circ$  suggests an internal to basal strength relation similar to that of simulation F2 ( $\phi = 30^\circ$ ,  $\phi_b = 10^\circ$ ) with a theoretical taper of  $3.4^\circ$ .

[61] The Makran, SE Iran and SW Pakistan (Figure 1b), is one of the largest accretionary wedges worldwide with more than 350 km in cross-sectional width and more than half of its area exposed on land [McCall, 2002]. The total taper is  $\sim 3.6^\circ$  [White and Ross, 1979]. Although the incoming sedimentary pile is  $\sim 7$  km thick, only the upper 4 km are involved in the frontal imbricate fan [Grando and McClay, 2007]. These upper levels are thrust along a weak horizon within the sedimentary sequence and the lower part is underplated. Platt et al. [1985] estimated that up to 50% of the incoming sediments have been underplated so that the lower sedimentary sequence was tectonically thickened by a factor of two to three. Underplating in the rear part of the wedge leads to surface uplift of the today onshore part [Ellouz-Zimmermann et al., 2007]. These observations can be explained by simulations with multiple frictional décollements, where the roof décollement is weaker than the basal one (Figure 11a, simulation DF3). Active roof-duplex and

antiformal stacking both push up the surface at the back of the simulation, producing a surface slope steeper than on areas where underplating is absent. This is consistent with the cross-sectional surface taper of the Makran, which, at its rear, is slightly steeper ( $\sim 1^\circ$ ) than in the coastal area ( $\sim 0.2^\circ$ ). The lower strength of the basal décollement relative to the wedge sequence can be explained by the exceptionally thick (7 km) incoming sediment sequence, as at a depth of 5 km, up to 90% of available smectite in shale is converted into illite [Bekins et al., 1994]. This process is accompanied by dehydration, which increases fluid pressure within the shale layers at deeper levels and thus weakens them. The probable absence of an intermediate décollement toward the rear explains the different wavelengths between the onshore and offshore Makran as well as recently active fault zones like the Ghasr Ghand Thrust (Figure 1b), which reaches down to the basal décollement as illustrated in simulation DF1 or DF2 in Figure 11a.

[62] The sub-Andean fold-and-thrust belt, NW Argentina (Figure 1c), is one of the active thin-skinned fold-and-thrust belts in a retroarc setting [Echavarría et al., 2003]. Décollement horizons follow Silurian shale at the base of the belt and upper Devonian shales within the stratigraphic sequence [Baby et al., 1992; Echavarría et al., 2003]. The intermediate décollement separates upper from lower structural levels. In the lower structural level, eastward verging in-sequence thrusts generate fault-bend anticlines with gentle backlimbs and steeper forelimbs. The upper structural level is characterized by folds with steep flanks and narrow crests (Figure 1c) [Echavarría et al., 2003]. These structural features are replicated in multiple frictional décollement simulations, where the basal décollement is weaker than the intermediate one (Figure 11a, simulation DF1). The lower stratigraphic level in simulation DF1 forms forward verging ramps with fault-bend anticlines. The upper level deformation is controlled by the intermediate décollement and builds steep flanking boxfold-shaped fault propagation folds.

[63] The Jura, NW Switzerland and E France (Figure 1d), is an Alpine fold belt displaced toward the NW over a salt décollement in middle and upper Triassic evaporites [e.g., Pfiffner et al., 1997]. This décollement can be tracked along the base of the Molasse Basin down to the crystalline roots of the Alps. During the late Alpine orogeny, the Molasse Basin acted as a stiff unit transferring shortening to its front, thus building the Jura Mountains [Pfiffner, 2009]. The southeastern part of the Jura, the Faltenjura, is characterized by closely grouped anticlines, whereas anticlines in the northwestern part, the Plateaujura, are separated by wide flat synclines [Pfiffner, 2009]. The thin-skinned sequence is 800 to 2000 m thick and the décollement evaporites had an initial thickness of  $< 500$  m [Sommaruga, 1997]. The structure of the Jura is best fitted by a single linear viscous décollement simulation with a viscosity of  $10^{18}$  Pa·s (Figure 9a, simulation V2). This simulation produced closely gathered anticlines at the rear of the evolving fold belt and solitary anticlines with flat, wide synclines in the distal part. These solitary anticlines can develop because the stresses can be easily transmitted horizontally through the sedimentary sequence, setting the whole pile under a similar state of stress (Figure 10b).

[64] The Parry Island fold belt in the western arctic islands, Canada (Figure 1e), is an ancient foreland fold-and-thrust belt attached to the Franklinian Mobile Belt, which results from the Late Devonian–Early Carboniferous collision of the Canadian and the Anabar–Aldan shields [Fox, 1985; Condie and Rosen, 1994; Harrison, 1995]. A lower décollement has been detected in evaporite and rock salt layers whose thickness is 60–2200 m; an upper shale layer has a thickness of up to 950 m. The overall width of the fold belt is  $\sim 200$  km after bulk shortening of  $<11\%$ , which indicates the relative weakness of the bottom décollement. The lower plastic sequence exhibits forward vergent and backward vergent ramp thrusts, locally building thrust stacks filling anticline cores of the upper sequence. The upper part shows upright anticlines and broad synclines, sporadically scattered by backward and frontward verging thrusts [Fox, 1985; Harrison, 1995]. Although the intermediate décollement level is formed of shale, the geological structures are consistent with simulations with two viscous décollements with a relatively high viscosity of  $10^{19}$  Pa·s (Figure 11b, simulation DV2). A decreased thickness of the basal salt décollement would have a similar effect. Basal thrusts would appear because the available salt volume would be too small to fill potentially growing anticlines.

[65] The Zagros belt, SW Iran (Figure 1f), results from postcollision shortening between the Arabian plate and the Iranian continental blocks [Mouthereau et al., 2007b]. The Zagros simply folded zone is characterized by a  $\sim 200$  km wide folded belt with mostly symmetrical open folds. The dominant wavelength of these folds is  $15.8 \pm 5.3$  km [Mouthereau et al., 2007a, 2007b]. Emami et al. [2010] defined two mobile levels within the stratigraphy. The lower mobile level lies right above the basement in the  $\sim 1$  km thick Hormuz evaporites. The upper mobile level is the  $\sim 800$  m thick Gachsaran evaporite. The measured wavelength and the fact that folding is the dominant shortening process is consistent with simulations exhibiting multiple viscous décollements with a salt viscosity of at most  $10^{18}$  Pa·s (Figure 11b, simulation DV3). The thickness of the viscous layer in this simulation matches the estimated thickness of the Hormuz evaporites [Emami et al., 2010]. An increase of the salt viscosity would decrease the ability of flexural slip between the upper and lower stratigraphic levels.

### 5.3. Comparison to Previous Modeling Studies

[66] The structural evolution of fold-and-thrust belts has been investigated in several analog and numerical modeling studies. Our numerical results are consistent with scaled analog models simulating the evolution of single décollement accretionary wedges. Regularly spaced thrust ramps develop in a forward vergent manner, each with minor backward vergent backthrusts at the leading edge, suggesting an initially conjugate fault system [e.g., Mulugeta, 1988; Storti and McClay, 1995; Schreurs et al., 2006]. We have determined a forward jump of the deformation front and documented steepening of thrust ramps during their integration into the growing wedge, in accordance with Figure 2 of Storti and McClay [1995]. They used sand with friction angles of  $\sim 29^\circ$  and  $23^\circ$ , respectively. Their resulting cross section looks alike our simulation F5 (Figure 6) with  $\varphi = 30^\circ$  and  $\varphi_b = 25^\circ$ .

[67] Several analog modeling studies investigate the influence of a viscous décollement on the structural evolution of a frictional rock sequence [e.g., Smit et al., 2003, 2010; Bahroudi and Koyi, 2003]. In contrast to purely frictional models, where deformation is dominated by forward verging in-sequence ramp systems, backthrusts and deformation gaps occur very frequently in modeled thrust belts over viscous décollements. Compression rate influences the structural evolution of the wedge sequence [Smit et al., 2003] due to the change of shear stress in the viscous layer (equation (11)).

[68] Konstantinovskaya and Malavieille [2011] have documented how an additional intermediate décollement promotes underplating and antiformal stacking of the bottom sequence. We numerically obtained a similar evolution with a second frictional décollement within the cover sequence. Underplating is most likely leading to antiformal stacks if the upper frictional décollement has a lower failure criterion (Figure 11, simulation DF3). Nalpas and Pichot [2009] and Couzens-Schultz et al. [2003] also investigated the structural effects of multiple décollement levels using a basal and upper, relatively thick viscous silicone layer. Their results and our numerical simulations with two viscous décollements are comparable (Figure 11b, simulation DV2).

[69] The mechanics of fold-and-thrust belts has been numerically investigated for more than two decades [Borja and Dreiss, 1989]. Studies focusing on the structural evolution of accretionary wedge-like systems overlying a single frictional décollement show in-sequence faulting with isolated thrusts forming in a piggyback manner [Strayer et al., 2001; Burbidge and Braun, 2002; Buitter et al., 2006; Simpson, 2006, 2011; Selzer et al., 2007; Stockmal et al., 2007; Miyakawa et al., 2010].

[70] Selzer et al. [2007] tested the effect of weak shear zones on the structural evolution of thrust belts. They obtained underplating and stacking at the rear when they applied a horizontally continuous weak inclusion, comparable to additional intersequential décollements in this study. Stockmal et al. [2007] presented an extensive study investigating the influence of multiple weak frictional décollements within a compressed sequence. In contrast to our study, they only address intersequential décollement layers weaker than the basal horizon, focusing on the influence of surface processes and strain weakening. Stockmal et al. [2007] achieve similar results as ours in terms of thrust sheet wavelength, antiformal stacking and restriction of deformation to the upper structural level above a very weak intersequential layer. The latter authors also agree with the critical wedge theory with respect to the total wedge scale.

[71] Simpson [2009, 2010] applied a viscous versus frictional substratum as décollement. Decreasing the viscosity in the basal layer suppressed the formation of in-sequence, forward vergent thrusts and stimulated the occurrence of backthrusts and single-standing folds. This was also obtained in the models presented here. Yamato et al. [2011] have shown that folding is promoted if the sedimentary sequence contains several viscous décollements. We obtained a similar response (Figure 11b, simulation DV3). Simpson [2011] argued that the critical wedge theory is not fully applicable because differential stresses out of localized strain zones are at a subcritical state and principal stress directions can strongly vary within a wedge. However, in our

understanding, the critical wedge theory does define an overall near-failure state of stress in a wedge; this depends on both the internal wedge properties and the bottom shear resistance and is independent from internal deformation processes. Our simulations underline the robustness of the critical wedge theory concerning critical taper angles (Figure 5) and principle stress orientations (Figure 6).

## 6. Conclusion

[72] A 2-D finite element numerical model with a viscoelastoplastic rheology was used to investigate the difference between fold-and-thrust belts overlying either a (linear and nonlinear viscous) salt or a (frictional) shale décollement and the influence of additional intermediate weak layers. Simulations with single frictional décollements lead to forward verging in-sequence thrusting forming ramps with dip angles depending on the wedge-internal stress directions. Viscous décollements lead to backward and forward verging thrusts equally, not forming a typical imbricate fan. This also leads to solitary box folds like those of the Jura Mountains. Nevertheless, simulations with either a viscous or a frictional décollement are both consistent with the critical wedge theory, concerning surface taper angles and internal principal stress directions.

[73] Intermediate décollements strongly influence the structural evolution of fold-and-thrust belts. In the case of frictional décollement style, the strength relation between the basal and the intersequential décollement is the main factor influencing the structural evolution of a fold-and-thrust belt. This strength relation likely is the cause of underplating and antiformal stacking as well as the installation of fault propagation folds. Intersequential viscous décollements support flexural slip within a layered rock pile, which enhances folding for low Newtonian viscosities ( $10^{18}$  Pa·s). For higher viscosities, layer-parallel gliding leads to detachment folds and fault propagation folds in the upper part. Simulations with power law salt rheology ( $n = 5$ ) indicated viscosities between  $4 \cdot 10^{18}$  and  $5 \cdot 10^{19}$  Pa·s for the basal, and approximately one order of magnitude higher for intermediate décollements at  $50^\circ\text{C}$ .

[74] Modeled structural styles reflect natural fold-and-thrust belts: underplating in the Makran accretionary wedge indicates the existence of an intermediate décollement weaker than the main sole thrust. We also conclude that the basal décollement was weaker than the intermediate one during the structural evolution of the sub-Andean thrust belt. Solitary box folds in the Jura and folding-dominated crustal deformation in the Zagros both point to salt viscosities of  $\sim 10^{18}$  Pa·s.

[75] **Acknowledgments.** We thank Stefano Tavani and Ritske Huisman for their valuable comments on the manuscript. This work was supported by Swiss National Fonds grant 2-77644-09. Boris Kaus was supported by starting grant 258830 from the European Research Council.

## References

- Baby, P., G. Herail, R. Salinas, and T. Sempere (1992), Geometry and kinematic evolution of passive roof duplexes deduced from cross-section balancing: Example from the foreland thrust system of the southern Bolivian sub-Andean zone, *Tectonics*, *11*(3), 523–536, doi:10.1029/91TC03090.
- Bahroudi, A., and H. A. Koyi (2003), Effect of spatial distribution of Hormuz salt on deformation style in the Zagros fold and thrust belt: An analog modelling approach, *J. Geol. Soc.*, *160*, 719–733, doi:10.1144/0016-764902-135.
- Baker, D. M., R. J. Lillie, R. S. Yeats, G. D. Johnson, M. Yousuf, and A. S. H. Zamin (1988), Development of the Himalayan frontal thrust zone: Salt Range, Pakistan, *Geology*, *16*(1), 3–7, doi:10.1130/0091-7613(1988)016<0003:DOTHFT>2.3.CO;2.
- Barnes, P. M., G. Lamarche, J. Bialas, S. Henrys, I. Pecher, G. L. Netzeband, J. Greinert, J. J. Mountjoy, K. Pedley, and G. Crutchley (2010), Tectonic and geological framework for gas hydrates and cold seeps on the Hikurangi subduction margin, New Zealand, *Mar. Geol.*, *272*(1–4), 26–48, doi:10.1016/j.margeo.2009.03.012.
- Bekins, B., A. M. McCaffrey, and S. J. Dreiss (1994), Influence of kinetics on the smectite to illite transition in the Barbados accretionary prism, *J. Geophys. Res.*, *99*(B9), 18,147–18,158, doi:10.1029/94JB01187.
- Berberian, M. (1983), The southern Caspian: A compressional depression floored by a trapped, modified oceanic crust, *Can. J. Earth Sci.*, *20*(2), 163–183, doi:10.1139/e83-015.
- Bingham, E. (1922), *Fluidity and Plasticity*, 462 pp., McGraw-Hill, New York.
- Biot, M. A. (1961), Theory of folding of stratified viscoelastic media and its implications in tectonics and orogenesis, *Geol. Soc. Am. Bull.*, *72*(11), 1595–1620, doi:10.1130/0016-7606(1961)72[1595:TOFOSV]2.0.CO;2.
- Bonini, M. (2007), Deformation patterns and structural vergence in brittle-ductile thrust wedges: An additional analog modelling perspective, *J. Struct. Geol.*, *29*(1), 141–158, doi:10.1016/j.jsg.2006.06.012.
- Borja, R. I., and S. J. Dreiss (1989), Numerical modeling of accretionary wedge mechanics: Application to the Barbados subduction problem, *J. Geophys. Res.*, *94*(B7), 9323–9339, doi:10.1029/JB094iB07p09323.
- Bourrouilh, R., J. P. Richert, and G. Zolnai (1995), The North Pyrenean Aquitaine Basin, France: Evolution and hydrocarbons, *AAPG Bull.*, *79*(6), 831–853.
- Boyer, S. E., and D. Elliott (1982), Thrust systems, *AAPG Bull.*, *66*(9), 1196–1230.
- Buiter, S. J. H., A. Y. Babeyko, S. Ellis, T. V. Gerya, B. J. P. Kaus, A. Kellner, G. Schreurs, and Y. Yamada (2006), The numerical sandbox: Comparison of model results for a shortening and an extension experiment, *Geol. Soc. Spec. Publ.*, *253*, 29–64, doi:10.1144/GSL.SP.2006.253.01.02.
- Burbidge, D. R., and J. Braun (2002), Numerical models of the evolution of accretionary wedges and fold-and-thrust belts using the distinct-element method, *Geophys. J. Int.*, *148*(3), 542–561, doi:10.1046/j.1365-246x.2002.01579.x.
- Burg, J. P., A. Dolati, D. Bernoulli, and J. Smit (2011), Structural style of the Makran Tertiary accretionary complex in SE-Iran, *GeoArabia*, in press.
- Buxtorf, A. (1916), Prognosen und befunde beim hauenstein—Und grenchenberg-tunnel und die bedeutung der letzteren fuer die geologie des juragebirges, *Verh. Naturforsch. Ges. Basel*, *27*, 184–254.
- Chemia, Z., H. Koyi, and H. Schmeling (2008), Numerical modelling of rise and fall of a dense layer in salt diapirs, *Geophys. J. Int.*, *172*(2), 798–816, doi:10.1111/j.1365-246X.2007.03661.x.
- Chemia, Z., H. Schmeling, and H. Koyi (2009), The effect of the salt viscosity on future evolution of the Gorleben salt diapir, Germany, *Tectonophysics*, *473*(3–4), 446–456, doi:10.1016/j.tecto.2009.03.027.
- Condie, K. C., and O. M. Rosen (1994), Laurentia-Siberia connection revisited, *Geology*, *22*(2), 168–170, doi:10.1130/0091-7613(1994)022<0168:LSCR>2.3.CO;2.
- Cooper, M. (2007), Structural style and hydrocarbon prospectivity in fold and thrust belts: A global review, *Geol. Soc. Spec. Publ.*, *272*, 447–472, doi:10.1144/GSL.SP.2007.272.01.23.
- Costa, E., and B. C. Vendeville (2002), Experimental insights on the geometry and kinematics of fold-and-thrust belts above weak, viscous evaporitic décollement, *J. Struct. Geol.*, *24*(11), 1729–1739, doi:10.1016/S0191-8141(01)00169-9.
- Couzens-Schultz, B. A., B. C. Vendeville, and D. V. Wiltschko (2003), Duplex style and triangle zone formation: Insights from physical modeling, *J. Struct. Geol.*, *25*(10), 1623–1644, doi:10.1016/S0191-8141(03)00004-X.
- Dabrowski, M., M. Krotkiewski, and D. W. Schmid (2008), MILAMIN: MATLAB-based finite element method solver for large problems, *Geochem. Geophys. Geosyst.*, *9*, Q04030, doi:10.1029/2007GC001719.
- Dahlen, F. A. (1984), Noncohesive critical Coulomb wedges: An exact solution, *J. Geophys. Res.*, *89*, 125–133.
- Dahlen, F. A., J. Suppe, and D. Davis (1984), Mechanics of fold-and-thrust belts and accretionary wedges: Cohesive Coulomb theory, *J. Geophys. Res.*, *89*, 87–101.
- Davis, D. M., and T. Engelder (1985), The role of salt in fold-and-thrust belts, *Tectonophysics*, *119*(1–4), 67–88, doi:10.1016/0040-1951(85)90033-2.
- Davis, D., J. Suppe, and F. A. Dahlen (1983), Mechanics of fold-and-thrust belts and accretionary wedges, *J. Geophys. Res.*, *88*, 1153–1172.

- Echavarría, L., R. Hernandez, R. Allmendinger, and J. Reynolds (2003), Subandean thrust and fold belt of northwestern Argentina: Geometry and timing of the Andean evolution, *AAPG Bull.*, 87(6), 965–985, doi:10.1306/01200300196.
- Ellouzi-Zimmermann, N., E. Deville, C. Muller, S. Lallemand, A. B. Subhani, and A. R. Tabreez (2007), Impact of sedimentation on convergent margin tectonics: Example of the Makran accretionary prism (Pakistan), in *Thrust Belts and Foreland Basins: From Fold Kinematics to Hydrocarbon Systems*, *Frontiers Earth Sci.*, vol. 5, pp. 327–350, Springer, Berlin.
- Emami, H., J. Verges, T. Nalpas, P. Gillespie, I. Sharp, R. Karpuz, E. P. Blanc, and M. G. H. Goodarzi (2010), Structure of the mountain front flexure along the Anaran anticline in the Pusht-e Kuh arc (NW Zagros, Iran): Insights from sand box models, *Geol. Soc. Spec. Publ.*, 330, 155–178, doi:10.1144/SP330.9.
- Fischer, G. J., and M. S. Paterson (1989), Dilatancy during rock deformation at high-temperatures and pressures, *J. Geophys. Res.*, 94(B12), 17,607–17,617, doi:10.1029/JB094iB12p17607.
- Fox, F. G. (1985), Structural geology of the Parry Islands fold belt, *Bull. Can. Pet. Geol.*, 33(3), 306–340.
- Glodny, J., J. Lohrmann, H. Ehtler, K. Grafe, W. Seifert, S. Collao, and O. Figueroa (2005), Internal dynamics of a paleoaccretionary wedge: Insights from combined isotope tectonochronology and sandbox modelling of the South-Central Chilean forearc, *Earth Planet. Sci. Lett.*, 231(1–2), 23–39, doi:10.1016/j.epsl.2004.12.014.
- Grando, G., and K. McClay (2007), Morphotectonics domains and structural styles in the Makran accretionary prism, offshore Iran, *Sediment. Geol.*, 196(1–4), 157–179, doi:10.1016/j.sedgeo.2006.05.030.
- Grelaud, S., W. Sassi, D. F. de Lamotte, T. Jaswal, and F. Roure (2002), Kinematics of eastern Salt Range and South Potwar Basin (Pakistan): A new scenario, *Mar. Pet. Geol.*, 19(9), 1127–1139, doi:10.1016/S0264-8172(02)00121-6.
- Harrison, J. C. (1995), Tectonics and kinematics of a foreland folded belt influenced by salt, Arctic Canada, *AAPG Mem.*, 65, 379–412.
- Hessami, K., H. A. Koyi, C. J. Talbot, H. Tabasi, and E. Shabanian (2001), Progressive unconformities within an evolving foreland fold-thrust belt, Zagros Mountains, *J. Geol. Soc.*, 158, 969–981, doi:10.1144/0016-764901-007.
- Ings, S. J., and C. Beaumont (2010), Continental margin shale tectonics: Preliminary results from coupled fluid-mechanical models of large-scale delta instability, *J. Geol. Soc.*, 167(3), 571–582, doi:10.1144/0016-76492009-052.
- Kaus, B. J. P. (2010), Factors that control the angle of shear bands in geodynamic numerical models of brittle deformation, *Tectonophysics*, 484(1–4), 36–47, doi:10.1016/j.tecto.2009.08.042.
- Kocher, T., S. M. Schmalholz, and N. S. Mancktelow (2006), Impact of mechanical anisotropy and power-law rheology on single layer folding, *Tectonophysics*, 421, 71–87, doi:10.1016/j.tecto.2006.04.014.
- Konstantinovskaya, E., and J. Malavieille (2011), Thrust wedges with decollement levels and syntectonic erosion: A view from analog models, *Tectonophysics*, 502(3–4), 336–350, doi:10.1016/j.tecto.2011.01.020.
- Kopf, A., and K. M. Brown (2003), Friction experiments on saturated sediments and their implications for the stress state of the Nankai and Barbados subduction thrusts, *Mar. Geol.*, 202(3–4), 193–210, doi:10.1016/S0025-3227(03)00286-X.
- Laubscher, H. (1992), Jura kinematics and the Molasse Basin, *Eclogae Geol. Helv.*, 85(3), 653–675.
- Lewis, K. B., and J. R. Pettinga (1993), The emerging, imbricate frontal wedge of the Hikurangi margin, in *Sedimentary Basins of the World*, vol. 2, *South Pacific Sedimentary Basins*, edited by P. F. Balance, pp. 225–250, Elsevier, Amsterdam.
- Li, S., S. Abe, L. Reuning, S. Becker, J. L. Urai, and P. Kukla (2012), Numerical modeling of the displacement and deformation of embedded rock bodies during salt tectonics: A case study from the South Oman salt basin, *Geol. Soc. Spec. Publ.*, 363, 503–520.
- Marques, F. O., L. Burlini, and J. P. Burg (2011), Microstructure and mechanical properties of halite/coarse muscovite synthetic aggregates deformed in torsion, *J. Struct. Geol.*, 33(4), 624–632, doi:10.1016/j.jsg.2011.01.003.
- McCall, G. J. H. (2002), A summary of the geology of the Iranian Makran, *Geol. Soc. Spec. Publ.*, 195, 147–204.
- McClay, K. (Ed.) (1992), *Thrust Tectonics*, 447 pp., Chapman and Hall, College Station, Tex.
- McClay, K. R., P. S. Whitehouse, T. Dooley, and A. Richards (2004), 3D evolution of fold and thrust belts formed by oblique convergence, *Mar. Pet. Geol.*, 21(7), 857–877, doi:10.1016/j.marpetgeo.2004.03.009.
- Miyakawa, A., Y. Yamada, and T. Matsuoka (2010), Effect of increased shear stress along a plate boundary fault on the formation of an out-of-sequence thrust and a break in surface slope within an accretionary wedge, based on numerical simulations, *Tectonophysics*, 484(1–4), 127–138, doi:10.1016/j.tecto.2009.08.037.
- Moresi, L., S. Quenette, V. Lemiale, C. Meriaux, B. Appelbe, and H. B. Muhlhans (2007), Computational approaches to studying non-linear dynamics of the crust and mantle, *Phys. Earth Planet. Inter.*, 163(1–4), 69–82, doi:10.1016/j.pepi.2007.06.009.
- Morley, C. K., R. King, R. Hillis, M. Tingay, and G. Backe (2011), Deep-water fold and thrust belt classification, tectonics, structure and hydrocarbon prospectivity: A review, *Earth Sci. Rev.*, 104(1–3), 41–91, doi:10.1016/j.earscirev.2010.09.010.
- Motiei, H. (1993), *Geology of Iran: Stratigraphy of Zagros*, 536 pp., Geol. Surv. of Iran, Tehran.
- Mouthereau, F., O. Lacombe, and B. Meyer (2006), The Zagros folded belt (Fars, Iran): Constraints from topography and critical wedge modelling, *Geophys. J. Int.*, 165(1), 336–356.
- Mouthereau, F., O. Lacombe, J. Tensi, N. Bellahsen, S. Kargar, and K. Amrouh (2007a), Mechanical constraints on the development of the Zagros folded belt (Fars), in *Thrust Belts and Foreland Basins: From Fold Kinematics to Hydrocarbon Systems*, *Frontiers Earth Sci.*, vol. 5, 247–266, Springer, Berlin.
- Mouthereau, F., J. Tensi, N. Bellahsen, O. Lacombe, T. De Boisgrollier, and S. Kargar (2007b), Tertiary sequence of deformation in a thin-skinned/thick-skinned collision belt: The Zagros folded belt (Fars, Iran), *Tectonics*, 26, TC5006, doi:10.1029/2007TC002098.
- Mukherjee, S., C. J. Talbot, and H. A. Koyi (2010), Viscosity estimates of salt in the Hormuz and Namakdan salt diapirs, Persian Gulf, *Geol. Mag.*, 147(04), 497–507, doi:10.1017/S001675680999077X.
- Mulugeta, G. (1988), Modeling the geometry of Coulomb thrust wedges, *J. Struct. Geol.*, 10(8), 847–859, doi:10.1016/0191-8141(88)90099-5.
- Nalpas, T., and T. Pichot (2009), Influence of synkinematic sedimentation in a thrust system with two decollement levels; analog modelling, *Tectonophysics*, 473(3–4), 466–475.
- Nettleton, L. L. (1934), Fluid mechanics of salt domes, *AAPG Bull.*, 18, 1175–1204.
- Pfiffner, A. (2009), *Geologie der Alpen*, 1st ed., Haupt, Berne.
- Pfiffner, O. A., P.-F. Erard, and M. Stauble (1997), Two cross-sections through the Swiss Molasse Basin (lines E4–E6, W1, W7–W10), in *Deep Structure of the Swiss Alps: Results of NRP 20*, edited by O. A. Pfiffner et al., pp. 139–153, Birkhauser, Basel, Switzerland.
- Platt, J. P. (1990), Thrust mechanics in highly overpressured accretionary wedges, *J. Geophys. Res.*, 95(B6), 9025–9034, doi:10.1029/JB095iB06p09025.
- Platt, J. P., J. K. Leggett, J. Young, H. Raza, and S. Alam (1985), Large-scale sediment underplating in the Makran accretionary prism, southwest Pakistan, *Geology*, 13(7), 507–511, doi:10.1130/0091-7613(1985)13<507:LSUITM>2.0.CO;2.
- Poblet, J., and R. J. Lisle (2011), Kinematic evolution and structural styles of fold-and-thrust belts, *Geol. Soc. Spec. Publ.*, 349, 1–24, doi:10.1144/SP349.1.
- Saffer, D. M., and B. A. Bekins (2006), An evaluation of factors influencing pore pressure in accretionary complexes: Implications for taper angle and wedge mechanics, *J. Geophys. Res.*, 111, B04101, doi:10.1029/2005JB003990.
- Saffer, D. M., K. M. Frye, C. Marone, and K. Mair (2001), Laboratory results indicating complex and potentially unstable frictional behavior of smectite clay, *Geophys. Res. Lett.*, 28(12), 2297–2300, doi:10.1029/2001GL012869.
- Schlüter, H. U., A. Prexl, C. Gaedicke, H. Roeser, C. Reichert, H. Meyer, and C. von Daniels (2002), The Makran accretionary wedge: Sediment thicknesses and ages and the origin of mud volcanoes, *Mar. Geol.*, 185(3–4), 219–232, doi:10.1016/S0025-3227(02)00192-5.
- Schmid, D. W., and Y. Y. Podladchikov (2006), Fold amplification rates and dominant wavelength selection in multilayer stacks, *Philos. Mag.*, 86(21–22), 3409–3423, doi:10.1080/14786430500380175.
- Schreurs, G., et al. (2006), Analog benchmarks of shortening and extension experiments, *Geol. Soc. Spec. Publ.*, 253, 1–27, doi:10.1144/GSL.SP.2006.253.01.01.
- Selzer, C., S. J. H. Buitert, and O. A. Pfiffner (2007), Sensitivity of shear zones in orogenic wedges to surface processes and strain softening, *Tectonophysics*, 437(1–4), 51–70, doi:10.1016/j.tecto.2007.02.020.
- Simpson, G. D. H. (2006), Modelling interactions between fold-thrust belt deformation, foreland flexure and surface mass transport, *Basin Res.*, 18(2), 125–143, doi:10.1111/j.1365-2117.2006.00287.x.
- Simpson, G. D. H. (2009), Mechanical modelling of folding versus faulting in brittle-ductile wedges, *J. Struct. Geol.*, 31(4), 369–381, doi:10.1016/j.jsg.2009.01.011.
- Simpson, G. D. H. (2010), Influence of the mechanical behaviour of brittle-ductile fold-thrust belts on the development of foreland basins, *Basin Res.*, 22(2), 139–156, doi:10.1111/j.1365-2117.2009.00406.x.

- Simpson, G. D. H. (2011), Mechanics of non-critical fold-thrust belts based on finite element models, *Tectonophysics*, 499(1–4), 142–155, doi:10.1016/j.tecto.2011.01.004.
- Smit, J. H. W., J. P. Brun, and D. Sokoutis (2003), Deformation of brittle-ductile thrust wedges in experiments and nature, *J. Geophys. Res.*, 108(B10), 2480, doi:10.1029/2002JB002190.
- Smit, J., J. P. Burg, A. Dolati, and D. Sokoutis (2010), Effects of mass waste events on thrust wedges: Analog experiments and application to the Makran accretionary wedge, *Tectonics*, 29, TC3003, doi:10.1029/2009TC002526.
- Sommaruga, A. (1997), Geology of the central Jura and the Molasse basin: New insights into an evaporite-based foreland fold and thrust belt, PhD thesis, Univ. de Neuchâtel, Neuchâtel, Switzerland.
- Sommaruga, A. (1999), Decollement tectonics in the Jura foreland fold-and-thrust belt, *Mar. Pet. Geol.*, 16(2), 111–134, doi:10.1016/S0264-8172(98)00068-3.
- Spiers, C. J., P. M. T. M. Schutjens, R. H. Brzesowsky, C. J. Peach, J. L. Liezenberg, and H. J. Zwart (1990), Experimental-determination of constitutive parameters governing creep of rock salt by pressure solution, *Deformation Mechanisms, Rheology and Tectonics, Geol. Soc. Spec. Publ.*, 54, 215–227.
- Stockmal, G. S., C. Beaumont, M. Nguyen, and B. Lee (2007), Mechanics of thin-skinned fold-and-thrust belts: Insights from numerical models, *Spec. Pap. Geol. Soc. Am.*, 433, 63–98.
- Storti, F., and K. McClay (1995), Influence of syntectonic sedimentation on thrust wedges in analog models, *Geology*, 23(11), 999–1002, doi:10.1130/0091-7613(1995)023<0999:IOSSOT>2.3.CO;2.
- Strayer, L. M., P. J. Hudleston, and L. J. Lorig (2001), A numerical model of deformation and fluid-flow in an evolving thrust wedge, *Tectonophysics*, 335(1–2), 121–145, doi:10.1016/S0040-1951(01)00052-X.
- Takahashi, M., K. Mizoguchi, K. Kitamura, and K. Masuda (2007), Effects of clay content on the frictional strength and fluid transport property of faults, *J. Geophys. Res.*, 112, B08206, doi:10.1029/2006JB004678.
- Tavani, S., and J. A. Munoz (2012), Mesozoic rifting in the Basque-Cantabrian Basin (Spain): Inherited faults, transversal structures and stress perturbation, *Terra Nova*, 24(1), 70–76, doi:10.1111/j.1365-3121.2011.01040.x.
- Turcotte, D., and G. Schubert (2002), *Geodynamics*, 2nd ed., Cambridge Univ. Press, New York.
- Urai, J. L., Z. Schlöder, C. J. Spiers, and P. Kukla (2008), Flow and transport properties of salt rocks, in *Dynamics of Complex Intracontinental Basins: The Central European Basin System*, edited by R. Littke et al., pp. 277–290, Springer, Berlin.
- Vermeer, P. A., and R. De Borst (1984), *Non-Associated Plasticity for Soils, Concrete and Rock*, 63 pp., Delft Univ. of Technol., Delft, Netherlands.
- Vernant, P., et al. (2004), Present-day crustal deformation and plate kinematics in the Middle East constrained by GPS measurements in Iran and northern Oman, *Geophys. J. Int.*, 157(1), 381–398, doi:10.1111/j.1365-246X.2004.02222.x.
- Wang, C. Y., N. H. Mao, and F. T. Wu (1980), Mechanical-properties of clays at high-pressure, *J. Geophys. Res.*, 85, 1462–1468.
- Westbrook, G. K., J. W. Ladd, P. Buhl, N. Bangs, and G. J. Tiley (1988), Cross-section of an accretionary wedge: Barbados Ridge complex, *Geology*, 16(7), 631–635, doi:10.1130/0091-7613(1988)016<0631:CSOAAW>2.3.CO;2.
- White, R. S., and D. A. Ross (1979), Tectonics of the western Gulf of Oman, *J. Geophys. Res.*, 84, 3479–3489.
- Yamato, P., B. J. P. Kaus, F. Mouthereau, and S. Castelltort (2011), Dynamic constraints on the crustal-scale rheology of the Zagros fold belt, Iran, *Geology*, 39(9), 815–818, doi:10.1130/G32136.1.